Journal of Controlled Release 392 (2026) 114726

Contents lists available at ScienceDirect

Journal of Controlled Release

journal homepage: www.elsevier.com/locate/jconrel

Effect of clinically relevant iron oxide nanoparticles on macrophage polarization, tumor growth and tumor microenvironment modulation

Karolin Roemhild [a,b,1], Yanchen Li [a,1], Roman A. Barmin [a], Seyed Mohammadali Dadfar [a,c], Ekaterina Savina [a], Kim Lindelauf [a], Diana Moeckel [a], Elena Rama [a], Teresa Lemainque [a,d], Finn von Maltzahn [a], Sven Thoröe-Boveleth [e], Robert Pola [f], Tomas Etrych [f], Ruth Knuechel-Clarke [b], Peter Boor [b,g], Thomas Kraus [e], Volkmar Schulz [h], Jan Grimm [i], Fabian Kiessling [a], Saskia von Stillfried [b,g], Roger M. Pallares [a,*], Twan Lammers [a,g,*]

[a] Institute of Experimental Molecular Imaging, University Hospital RWTH Aachen, Aachen, Germany
[b] Institute of Pathology, University Hospital RWTH Aachen, Aachen, Germany
[c] Ardena Oss, Kloosterstraat 9, 5349 AB Oss, the Netherlands
[d] Department of Diagnostic and Interventional Radiology, Medical Faculty, University Hospital RWTH Aachen, Aachen, Germany
[e] Institute of Occupational, Social and Environmental Medicine, University Hospital RWTH Aachen, Aachen, Germany
[f] Institute of Macromolecular Chemistry, Czech Academy of Sciences, Prague, Czech Republic
[g] Center for Integrated Oncology Aachen Bonn Cologne Duesseldorf (CIO ABCD), Aachen, Germany
[h] Institute for Imaging and Computer Vision, University Hospital RWTH Aachen, Aachen, Germany
[i] Department of Radiology, Memorial Sloan Kettering Cancer Center, New York, NY, USA

ARTICLE INFO

Keywords:
Tumor microenvironment
Iron metabolism
Iron oxide nanoparticles
SPION
Macrophage polarization
Magnetic resonance imaging

ABSTRACT

Macrophages are key regulators of the tumor microenvironment (TME) and attractive targets for nanomedicine therapies. Because intracellular iron can promote pro-inflammatory macrophage polarization, superparamagnetic iron oxide nanoparticles (SPION) have been proposed as potential antitumor therapeutics. Nevertheless, their ability to remodel the TME and inhibit tumor growth has remained unclear. Here, we evaluated whether the commercially available SPION formulations Feraheme and Synomag can regulate macrophage polarization, modulate the microenvironment, affect tumor growth, and alter tumor-targeted drug delivery. *In vitro*, despite being internalized by macrophages highly efficiently, Feraheme and Synomag only elicited modest effects on macrophage polarization markers. *In vivo*, repeated intravenous administrations of Feraheme in an orthotopic and syngeneic 4 T1 triple-negative breast cancer model resulted in significant increases in intratumoral iron levels. However, they did not affect tumor growth nor statistically significant altered tumor-associated macrophage density and polarization, T-cell subsets, or the composition of the TME. Accordingly, pre-treatment with Feraheme did not alter tumor vascularization or collagen content, nor did it result in a statistically significant improvement in the delivery of a model polymeric nanocarrier. Together, these results support the use of SPION as tracers for macrophage-targeted imaging applications rather than as antitumor therapeutics and TME priming agents.

1. Introduction

Superparamagnetic iron oxide nanoparticles (SPION) are extensively investigated for a broad spectrum of biomedical applications [1]. Originally developed as contrast agents for magnetic resonance imaging (MRI), particularly for the diagnostic evaluation of liver pathologies [2,3], their clinical use has since expanded into both diagnostic and therapeutic domains [4]. Today, SPION are approved for the intravenous treatment of severe anemia in patients who do not respond to oral supplementation [5–7]. Because of their physicochemical attributes and favorable *in vivo* behavior, they are additionally used or explored in magnetic cell sorting, cell labeling for magnetic particle imaging (MPI),

* Corresponding authors.
E-mail addresses: rmoltopallar@ukaachen.de (R.M. Pallares), tlammers@ukaachen.de (T. Lammers).
[1] These authors contributed equally to this work.

https://doi.org/10.1016/j.jconrel.2026.114726
Received 23 December 2025; Received in revised form 10 February 2026; Accepted 12 February 2026
Available online 13 February 2026
0168-3659/© 2026 The Authors. Published by Elsevier B.V. This is an open access article under the CC BY-NC-ND license (http://creativecommons.org/licenses/by-nc-nd/4.0/).

and magnetic fluid hyperthermia for cancers such as glioblastoma and pancreatic tumors [8–10].

When administered intravenously, SPION are typically rapidly cleared by the mononuclear phagocyte system, which mainly consists of macrophages in the liver, spleen, lungs, and lymph nodes [11,12]. Macrophages are key components of the innate immune system and play central roles in host defense and tissue homeostasis [13–15]. Their phenotypes vary widely depending on their activation state, with differences in receptor expression, cytokine secretion, and metabolic activity. Broadly, macrophages are often described along the M1-M2 spectrum, corresponding to classically activated (M1-like) and alternatively activated (M2-like) phenotypes. M1-like states are associated with inflammatory and antimicrobial activities, as well as antitumoral functions such as promoting cytotoxic immune activity, whereas M2-like states are linked to tissue repair and immunoregulation, although these categories are not strictly dichotomous, and functions can overlap [16,17].

In many cancers, including breast cancer, macrophages are key components of the tumor microenvironment (TME), and their abundance and M2 polarization often correlate negatively with prognosis [18]. Tumor-associated macrophages (TAM) are typically skewed toward an M2-like phenotype, which locally suppress antitumor immunity, stimulates angiogenesis, and remodels the extracellular matrix, thereby supporting cancer growth and invasion [19]. Because of their multifaceted roles in tumor progression, TME modulation, and responses to (immuno)therapy, TAM have emerged as promising targets for nanomedicine- and immunotherapy-based anticancer strategies [20–22].

Macrophages also play crucial roles in iron metabolism by mediating iron uptake and recycling [23]. Importantly, M1-like and M2-like macrophages differ markedly in how they process iron. Pro-inflammatory M1-like macrophages tend to retain iron, exhibiting reduced uptake and excretion but elevated intracellular iron storage. Anti-inflammatory M2-like macrophages display high iron turnover, characterized by increased uptake and release, and consequently maintain relatively low intracellular iron levels [24]. Reciprocally, iron itself can regulate macrophage fate and polarization. A few studies have demonstrated that iron loading promotes macrophage activation toward a pro-inflammatory phenotype and, consequently, the induction of an M1-like, antitumoral TAM profile [25–27], thereby enhancing antitumor immune responses. In particular, SPION have been shown to induce a pro-inflammatory phenotype, contributing to tumor growth delay when co-injected with breast cancer cells [11]. However, it remains unclear whether SPION can modulate TAM in pre-established tumors. Here, we deliberately focused on pre-established, palpable tumors to reflect a clinically relevant treatment scenario, rather than an early "window-of-opportunity" intervention.

Although a limited number of studies have employed clinically approved SPION such as Feraheme, these investigations were largely mechanistic and did not aim to comprehensively evaluate functional TAM reprogramming in established tumor models [28,29]. In contrast, the majority of previous studies investigating TAM modulation have relied on in-house–synthesized SPION formulations, leaving the translational relevance of clinically approved SPION insufficiently explored [30,31]. Repurposing clinically used imaging or therapeutic agents for a new application could improve the cost-efficiency of this approach.

This study investigates macrophage modulation induced by SPION *in vitro* and *in vivo*, exploring effects on tumor growth and the TME in an orthotopic and syngeneic 4 T1 triple-negative breast cancer mouse model. Importantly, we evaluated the antitumor efficacy and TME modulation in mice with pre-established 4 T1 tumors. *In vitro*, two commercial SPION, Feraheme and Synomag, showed time- and concentration-dependent macrophage uptake with good biocompatibility. However, both nanoparticles induced only modest effects on macrophage polarization in the murine macrophage cell line J774A.1 and in human monocyte-derived macrophages (hMDMs). *In vivo*, we assessed the effects of clinically used Feraheme in 4 T1 tumor-bearing BALB/c mice. SPION treatment increased intratumoral iron accumulation but did not alter tumor growth, proliferation, apoptosis, necrosis, TAM levels or polarization, T-cell composition, vascular or collagen features, or the tumor accumulation of a prototypic polymer-based drug delivery system. Multimodal *in vivo* and *ex vivo* imaging confirmed increased intratumoral iron pools following SPION administration, but revealed only marginal effects on tumor growth, TME remodeling, and tumor-targeted drug delivery.

2. Materials and methods

2.1. Materials

Potassium hexacyanoferrate(II), Nuclear Fast Red, and formaldehyde were purchased from Sigma-Aldrich (Munich, Germany); sodium hydroxide, nitric acid, hydrochloric acid, hydrogen peroxide, hexane, methanol, acetone, ethanol, diethyl ether, hematoxylin, acidified eosin, and Mowiol® 4–88 mounting medium were from Carl Roth (Karlsruhe, Germany); Vitroclud mounting medium was from R. Langenbrinck GmbH (Emmendingen, Germany); phosphate-buffered saline (PBS, pH 7.2), low-glucose DMEM, RPMI-1640, fetal bovine serum (FBS), and penicillin/streptomycin were provided by Thermo Fisher Scientific / Gibco (Dreieich, Germany); GeneMATRIX Universal RNA Purification Kit was obtained from EURx (Gdańsk, Poland); iScript™ cDNA Synthesis Kit was purchased from Bio-Rad (California, USA); recombinant human M-CSF, IFN-γ, and IL-4 were provided by PeproTech (Germany); TMR red *In-Situ* Cell Death Detection Kit based on terminal deoxynucleotidyl transferase-mediated dUTP nick-end labeling (TUNEL) was obtained from Roche (Germany); rabbit anti-mouse Ki67 antibody was from Abcam (Germany); secondary antibodies were obtained from Dianova (Germany); flow-cytometry antibodies and 7-AAD were purchased from BioLegend (California, USA); hydrogen peroxide (Suprapur, 65%), and the rhodium standard (1 mg/L) for inductively coupled plasma mass spectrometry (ICP-MS) were from Merck (Darmstadt, Germany); Synomag® and Feraheme® were obtained from micromod (Rostock, Germany) and AMAG Pharmaceuticals, Inc. (Waltham, MA, USA), respectively. Dy750-labeled poly(*N*-(2-hydroxypropyl)methacrylamide) (pHPMA) polymers were prepared as described previously [32,33]. Deionized water was used in all experiments and produced using a PURELAB flex 2 system (ELGA LabWater, Celle, Germany). All reagents were of appropriate analytical grade.

2.2. SPION characterization

SPION were characterized by dynamic light scattering (DLS) and transmission electron microscopy (TEM). Their hydrodynamic diameter and polydispersity index (PDI) were measured by DLS using a Zetasizer Nano-ZS instrument (Malvern Instruments, Malvern, U.K.). The samples were diluted in DI water before measurement, and the samples were measured in triplicate at a fixed scattering angle of 173°. The diluted nanoparticle dispersions were also left to absorb onto carbon-coated copper grids for TEM core size analysis. Images were acquired with a Zeiss 906 electron microscope (LEO, Oberkochen, Germany) operated at 60 kV.

2.3. In vitro assays

2.3.1. Cell culture of murine monocyte/ macrophage cell line J774A.1

The immortalized murine monocyte/ macrophage cell line J774A.1 was obtained from Sigma-Aldrich (St. Louis, US). Cells were cultured at 37 °C in a humidified atmosphere with 5% CO_2. Medium was supplemented with 1% penicillin/ streptomycin (10,000 U/mL penicillin; 10 mg/mL streptomycin, Life Technologies GmbH, Germany) and 10% fetal bovine serum (FBS, Life Technologies GmbH, Germany). J774A.1 cells were cultured in low-glucose DMEM (from Gibco, Life Technologies

GmbH, Germany).

2.3.2. Source, isolation, differentiation of hMDMs

Buffy coats were obtained from the Transfusion Medicine Department, University Hospital Aachen. Peripheral blood mononuclear cells (PBMC) were isolated by density-gradient centrifugation on Ficoll-Paque PLUS: buffy coat diluted 1:1 with PBS, layered on Ficoll, and centrifuged at room temperature for 25 min at 2000 rpm; interphase PBMC were collected, washed three times with PBS (10 min, 1200 rpm, room temperature), followed by a platelet-removal wash (10 min, 1000 rpm, room temperature). Cells were resuspended in serum-free medium, counted, seeded at ~3×10^6 cells/mL (2 mL per well; tissue-culture-untreated 6-well plates), and allowed to adhere for 1 h. After two PBS washes, differentiation media (RPMI-1640, 10% FBS, 1% penicillin/streptomycin) supplemented with human M-CSF (20 ng/mL) was added; monocytes were differentiated for 6 days before experiments. For polarization controls, cells were treated with lipopolysaccharide (LPS, Merck, Germany) (100 ng/mL) + interferon γ (IFNγ, Peprotech, Germany) (20 ng/mL) for 6 h (M1-like) or with interleukin 4 (IL-4, Peprotech, Germany) (20 ng/mL) for 24 h (M2-like) before readouts. Use of anonymized buffy coats was approved by the Ethics Committee, with informed consent from all donors.

2.3.3. Cell viability assay

XTT (*i.e.* 2,3-bis-(2-methoxy-4-nitro-5-sulfophenyl)-2H-tetrazolium-5-carboxanilide) assay was performed according to the manufacturer's instructions to assess the cytotoxicity of the investigated compounds. Briefly, 5×10^3 cells per well were seeded in 96-well plates and incubated overnight. The medium was removed, and the SPION dispersed in the medium were added. After 72 h, cells were washed with PBS, and 50 μL of XTT reagent was added, followed by a 2 h incubation. Absorbance was measured using a Tecan Infinite M200 plate reader. Viability was calculated as the percentage of viable cells relative to the untreated control cells. Experiments have been performed in triplicate.

2.3.4. Iron uptake analysis

Iron uptake was studied by Prussian blue staining and ICP-MS. For Prussian blue staining, cells were seeded onto coverslips in 24-well plates at a density of 2×10^5 cells per well and incubated overnight. The medium was removed, and the SPION were added in concentrations ranging from 0.01 to 1 mM. After incubating for 4 or 18 h, the medium was removed. The cells were fixed with 4% (*v/v*) formaldehyde solution at room temperature for 10 min, and after every step, they were washed once with PBS. A working solution was freshly prepared by mixing equal volumes of 2.5% (*w/v*) potassium hexacyanoferrate (II) and 2.5% (*v/v*) HCl. The solution was applied to the fixed cells for 10 min at room temperature, followed by counterstaining with Nuclear Fast Red (Sigma-Aldrich, St. Louis, US) for 5 min at room temperature. Cells were rinsed with DI water, mounted with Mowiol® 4–88 (Roth, Karlsruhe) on glass microscopy slides, and imaged on a Vectra 3.0 Automated Quantitative Pathology Imaging System (PerkinElmer, USA); images were exported with Phenochart 1.0.12. Experiments were performed in triplicate.

In parallel, cell lysates were analyzed by ICP-MS to quantify SPION uptake by macrophages. J774A.1 were seeded in 6-well plates at a density of 8×10^5 cells per well and incubated overnight. Primary macrophages were used after differentiation was completed after six days. The following day cells were treated with working concentrations of compounds prepared in medium for either 4 or 18 h. Afterward, cells were washed with PBS and harvested. The resulting cell pellet was dissolved in 1 mL HCl (20%, analytical grade in DI water) and further diluted in DI water (1:3). The measurements were performed by the Occupational, Social and Environmental Medicine Department (University Hospital Aachen) on an ICP-MS machine (8900-QQQ, Agilent, Waldbronn, Germany). Rhodium (1 mg/L, Merck, Darmstadt, Germany) was used as an internal standard for error correction.

2.3.5. Gene expression analysis

To investigate the macrophage polarization upon iron treatment, J774A.1 cells and primary human PBMC-derived cells were analyzed by quantitative polymerase chain reaction (qPCR). J774A.1 cells were seeded at a density of 8×10^5 cells per well in 6-well plates and incubated overnight. Primary macrophages were used after the differentiation was completed, after six days of incubation. The following day, cells were treated with working concentrations of the compounds prepared in cell medium for 18 h. Additional untreated samples were included in every experiment, serving as controls. The cells were treated with a combination of 100 ng/ mL LPS with 20 ng/ mL IFNγ for 6 h to induce pro-inflammatory polarized macrophages. For an anti-inflammatory macrophage phenotype, cells were incubated for 24 h with 20 ng/ mL IL-4. Experiments were performed in triplicate.

Next, according to manufacturer instructions, ribonucleic acid (RNA) was isolated using the GeneMATRIX Universal RNA Purification Kit (EURx, Gdańsk, P.L.). The RNA concentration was measured using the NanoDrop One (Thermo Fisher Scientific, Waltham, U.S.). The purified RNA was used as a template to produce complementary deoxyribonucleic acid (cDNA) according to the iScript cDNA Synthesis Kit (Bio-Rad, California, U.S.). Finally, qPCR was performed using a C1,000 Touch Thermal Cycler (Bio-Rad, California, U.S.). Primer pairs to determine macrophage polarization were purchased from Eurofins. The target gene and the corresponding primer pairs are summarized in Table S1 (human) and Table S2 (murine).

2.4. In vivo experiments

2.4.1. Tumor model, treatment, and anesthesia

Animal experiments were conducted following the German animal welfare regulations and were approved by the State Office for Nature, Environment and Consumer Protection of North Rhine-Westphalia (LANUV NRW) (AZ 84–02.04.2017.A045). Female BALB/cAnNRj mice (Janvier Labs, France) aged 10–12 weeks were housed under pathogen-free conditions with food and water *ad libitum* and a 12 h light-dark cycle. 4 T1 cells (2.5×10^4), a syngeneic and highly aggressive murine model of triple-negative breast cancer (TNBC) lacking estrogen receptor, progesterone receptor, and HER2 expression, were inoculated into the right abdominal mammary fat pad, and the tumors were grown for seven days. Subsequently, the mice were treated over two weeks with, in total, six intravenous iron administrations (30 mg/kg per treatment) or with either PBS or corresponding concentrations of the nanoparticle coating material (dextran) as controls [34,35]. Serial MRI was performed at baseline and on days 1, 6, and 11 after treatment start to localize tumors; after the sixth dose, hybrid μCT–fluorescence tomography tracked Cy7-pHPMA from 0.25 to 72 h. In total, ten animals per group were randomly assigned. All experimental procedures were performed under inhalation anesthesia using 2% (*v/v*) isoflurane. Five days before the optical imaging experiments, the diet was changed to chlorophyll-free food (Sniff Spezialdiäten GmbH, Germany) to reduce background fluorescence.

2.4.2. In vivo multimodal imaging

MRI was performed on a 7 T BioSpec small-animal system (Bruker, Germany) with a ^{1}H transmit–receive volume coil with an inner diameter of 4 cm at baseline (pre-treatment) and on days 1, 6, and 11 after therapy start.

Sequences and parameters were: T_2-weighted TurboRARE (repetition time = 1300 ms, echo time = 1300/25 ms, RARE factor = 8, echo spacing = 8.33 ms, number of averages = 8, slice thickness = 1 mm, matrix size = 256 × 256, FOV = 30 × 33 mm^2, 15 slices, total acquisition time = 5 min 33 s) and a multi-gradient echo sequence for T_2* mapping (repetition time = 2000 ms, echo time = 3 ms, flip angle = 50°, echo spacing = 5.50 ms, echo images = 30, number of averages = 2, slice thickness = 1 mm, matrix size = 144 × 112, FOV = 33 × 23 mm^2, 9 slices, total acquisition time = 5 min 36 s). T2* mapping used the

'mapshim' technique to homogenize the magnetic field in an ellipsoidal volume covering the abdomen, excluding air cavities. T2* relaxation times were retrieved by fitting an exponential decay function to the signal intensities SI(TE) = M_0 * exp.(−T2* times TE) per pixel/within a ROI covering the tumor using Paravision.

μCT was acquired on a U-CT OI system (MILabs, Utrecht, NL) using full-rotation step-and-shoot with 480 projections (1944 × 1536 px), 55 kV tube voltage, 0.17 mA current, and 75 ms exposure, and was reconstructed for tumor-volume quantification at the same time points; when used in hybrid microcomputed tomography-fluorescence tomography (μCT–FLT) mode, optical scans used ~130 scan points with 730 nm excitation and 775 nm detection.

2.5. Ex vivo analysis

2.5.1. Organ sampling for ex vivo analysis

Mouse organs and tumors were collected and divided into three parts. One part was embedded in TissueTek O.C.T. (Sakura Finetek Europe, The Netherlands) and stored at −80 °C; one part was formalin-fixed and paraffin-embedded (FFPE); and the third part was frozen at −80 °C for ICP-MS. ICP-MS measurements were performed using an Agilent 8900-QQQ (Waldbronn, Germany).

2.5.2. Prussian blue staining of tumor tissue

The FFPE tumor blocks were sectioned at 5 μm on an HM430 microtome (Thermo Fisher Scientific, Waltham, MA, USA), deparaffinized, and rehydrated to distilled water. The Prussian blue working solution was prepared as described before; slides were microwaved for 30 s and rested for 5 min at room temperature. Counterstaining with Nuclear Fast Red (Sigma-Aldrich, St. Louis, USA) was performed for 5 min at room temperature. Sections were dehydrated, cleared, and mounted with Vitroclud. Images were acquired on a Vectra 3.0 Automated Quantitative Pathology Imaging System (PerkinElmer, USA) and exported using Phenochart 1.0.12.

2.5.3. ICP-MS for tissue iron quantification

Tissues were completely digested using microwave pressure digestion in a 1:1:1:1 mixture of nitric acid, hydrochloric acid, hydrogen peroxide, and DI water, heated until complete digestion. Rhodium (1 mg/L) served as an internal standard. After complete dissolution, digests were diluted 1:10 with DI water and analyzed using an Agilent 8900-QQQ ICP-MS (Waldbronn, Germany).

2.5.4. Ki67 and TUNEL staining

Tumor cryosections (8 μm; CM3050S, Leica) were fixed with 4% formaldehyde for 15 min at room temperature. TUNEL was performed using the *In-Situ* Cell Detection Kit, TMR red (Roche, Germany). Proliferation was assessed with a rabbit anti-mouse Ki67 antibody (Abcam, Germany) and appropriate secondary antibodies (Dianova, Germany). Nuclei were counterstained with DAPI; sections were mounted in Mowiol® 4–88. Imaging was performed on an Axio Imager M2; quantification was performed using ImageJ.

2.5.5. Hematoxylin & Eosin (H&E) staining

FFPE tumor sections (5 μm) were H&E-stained on an automated stainer (Tissue-Tek Prisma Plus, Sakura Finetek) and coverslipped using a film-based coverslipping system (Tissue-Tek Film, Sakura Finetek). Slides were scanned at 40× on an Aperio AT2 whole-slide scanner (Leica Biosystems, Wetzlar, Germany). Image analysis was performed using Imalytics Preclinical (v2.1, Gremse IT, Germany). Necrotic regions were defined as areas lacking hematoxylin nuclear staining with loss of cellular detail; necrosis was quantified as area fraction in Imalytics. Three sections per tumor and five animals per group were evaluated.

2.5.6. Immunofluorescent staining

Eight μm tumor cryosections were cut on a CM3050S cryotome (Leica, Wetzlar, Germany). Three sections per tumor were fixed in 80% (*v/v*) methanol for 5 min, followed by cold acetone for 2 min. Primary monoclonal antibodies used: rat anti-mouse CD31/PECAM-1 (BD Biosciences, Germany; blood vessels), rat anti-mouse F4/80 (AbD Serotec, Germany; macrophages), rat anti-mouse CD206/Mrc1 (Acris Antibodies, Germany; anti-inflammatory macrophages), and rat anti-mouse CD86 (NOVUS, MO, USA; pro-inflammatory macrophages). Appropriate secondary antibodies were from Dianova (Germany). Nuclei were counterstained with DAPI and sections mounted in Mowiol® 4–88. Images were acquired on an Axio Imager M2 microscope and analyzed in ImageJ.

2.5.7. Flow cytometry for immunophenotyping

From the same specimens, tissues were allocated for flow cytometry. Tumors were minced and digested with Collagenase IV and DNase I for 30 min at 37 °C, filtered through a 70 μm cell strainer, and gently dispersed with a syringe plunger. Cell suspensions were washed and subjected to red blood cell lysis (for blood: 100 μL per mouse; RBC lysis repeated 3×). The liver and spleen were processed similarly without enzymatic digestion. Samples were stained with antibody panels (BioLegend, CA, USA; see Table S3, S4) in 100 μL fluorescence-activated cell sorting (FACS) buffer for 15 min on ice, washed, and labeled with 7-AAD for viability. Data were acquired on a BD FACSCanto II (BD, NJ, USA) at the Flow Cytometry Core Facility, University Clinic Aachen, and analyzed in FlowJo. Antibody panels and clones are listed in Table S3 (macrophage) and Table S4 (T-cell).

2.5.8. Two-photon laser scanning microscopy (TPLSM)

Cryopreserved tumors were sectioned at 70 μm and analyzed for collagen deposition, polymer accumulation, and blood-vessel density. Stacks of 50 images (z-step 1 μm) were acquired with a 25× water-immersion objective on an Olympus FV1000MPE multiphoton system (Olympus, Germany). Fluorescent polymers, vasculature (rhodamine-lectin), and collagen I/III (second-harmonic generation) were imaged in each stack. Images were analyzed in Imaris v9.3 (Bitplane AG, Switzerland).

2.6. Statistical analysis

Results are reported as mean ± standard deviation. Statistical analyses were performed using GraphPad Prism 10. One-way ANOVA followed by Tukey's *post hoc* multiple-comparisons test, or two-way ANOVA followed by Tukey's multiple-comparisons test, were applied as appropriate. *p*-values lower than 0.05 were considered as statistically significant; (ns), (*), (**), (***) and (****) indicate groups with $p > 0.05$, $p < 0.05$, $p < 0.01$, $p < 0.001$, and $p < 0.0001$, respectively.

3. Results

3.1. SPION characterization

We investigated two commercially available SPION formulations: Feraheme (ferumoxytol coated with carboxymethyl-dextran) and Synomag (multicore maghemite nanoparticles with a dextran-based coating). Feraheme is an FDA-approved intravenous iron replacement therapeutic that has also been repurposed off-label as an MRI contrast agent [4]. In contrast, Synomag is a research-grade formulation designed for high magnetic responsiveness and is commonly used in preclinical studies involving magnetic particle imaging and magnetic hyperthermia [36,37]. Together, these two formulations provide complementary platforms, since Feraheme is a clinically approved agent, while Synomag is a high-performance preclinical nanomedicine for emerging imaging and therapeutic strategies.

TEM characterization confirmed significant differences in core size between the two formulations, with Feraheme exhibiting smaller cores than Synomag (6.4 ± 1.1 *vs* 18.6 ± 4.4 nm; Fig. 1a and b). This trend

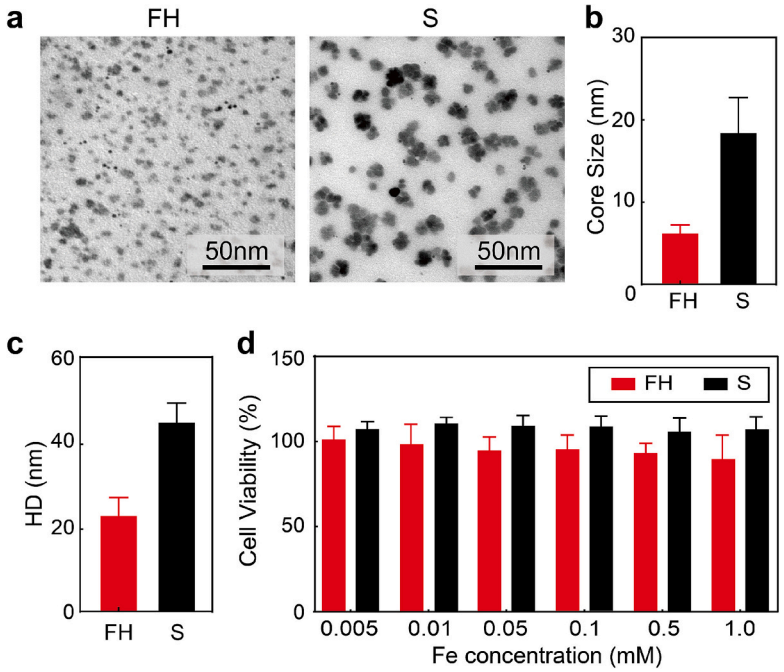


Fig. 1. Physicochemical characterization and cytocompatibility of SPION. (a) TEM micrographs (scale bars, 50 nm). (b) Core size quantified based on TEM micrographs (mean ± SD; $n = 3$). (c) Hydrodynamic diameter measured by DLS (mean ± SD; n = 3). (d) J774A.1 macrophage viability after 72 h exposure to increasing SPION concentrations (mean ± SD; n = 3 independent experiments, each in triplicate). Abbreviations: HD, hydrodynamic diameter; FH, Feraheme; S, Synomag.

aligned with the smaller hydrodynamic diameter of Feraheme, as measured by DLS (23 ± 3 *vs* 45 ± 5 nm; Fig. 1c), in agreement with previously reported values [38–40]. Moreover, *in vitro* biocompatibility screenings confirmed the high biocompatibility of both formulations in J774A.1 macrophages across a broad concentration range (0.01–1 mM Fe) commonly used during *in vitro* SPION studies (Fig. 1d). This range corresponds to ~0.6–56 mg Fe/L and was selected to cover low-to-moderate exposure levels relative to blood concentrations reported for clinically administered Feraheme [41–43]. Therefore, both SPION were subsequently evaluated in macrophage uptake and polarization studies.

3.2. SPION macrophage uptake is time-, concentration- and particle type-dependent

SPION are reported to affect cellular behavior, including that of phagocytes, through uptake-dependent alterations in metabolic and signaling pathways [44]. Based on published reports showing rapid macrophage uptake of SPION within hours, with near-maximal uptake reached by ~12 h and later cellular responses commonly assessed at 18–24 h [45–50], we selected 4 h and 18 h as representative early and late exposure time points across the tested iron concentration range (0.01–1 mM Fe). The murine macrophage cell line J774A.1 and primary human monocyte-derived macrophages (hMDM) were used to evaluate formulation-specific and interspecies differences. Intracellular iron was visualized and quantified using Prussian blue staining, and total cellular iron content was measured by ICP-MS.

As expected, intracellular iron levels increased with both concentration and exposure time for all conditions. In good agreement with previous reports, SPION uptake was readily detectable at 4 h and further increased at 18 h in both macrophage models. Notably, Feraheme displayed greater iron uptake than Synomag in both macrophage models. For example, in J774A.1 cells exposed to 1 mM Fe, Feraheme resulted in approximately 3- and 9-times higher iron internalization after 4 and 18 h, respectively (Fig. 2a and b). A similar trend was observed in hMDMs, although overall iron accumulation was (on average) 5-times lower (Fig. 2c and d), consistent with the higher and faster baseline phagocytic activity of the murine cell line [51,52].

It is important to note that both formulations were administered at equivalent iron concentrations, as it is standard in inorganic nanomedicine studies. Because Feraheme particles are (hydrodynamically) smaller, this dosing strategy introduces a greater number of particles injected over Synomag. Moreover, both formulations had slightly different coating material involved, hence, surface chemistry may also contribute to the observed changes. Therefore, this combination of formulation-dependent differences likely favored the higher net iron accumulation observed with Feraheme.

3.3. In vitro macrophage polarization remains largely unchanged upon SPION treatment

After confirming the successful internalization of both SPION formulations in the two cell models, we next explored their impact on macrophage polarization at two iron concentrations (0.01 and 0.1 mM Fe) after 18 h of exposure. RT-qPCR analysis was performed to quantify the expression of the key pro-inflammatory markers interleukin-1β (IL-1β), tumor necrosis factor-alpha (TNFα), C-X-C motif chemokine ligand (CXCL) 10, and inducible nitric oxide synthase (iNOS), as well as the anti-inflammatory markers arginase 1 (Arg1) and CD206. LPS combined with IFNγ and IL-4 were used as positive controls to induce M1-like pro-inflammatory and M2-like anti-inflammatory phenotypes, respectively. In J774A.1 cells, LPS/IFNγ treatment led to a robust up-regulation (between 2 and 5 orders of magnitude) of all four pro-inflammatory biomarkers examined (Fig. 3a). As expected, IL-4 stimulation markedly increased Arg1 expression and, to a lesser extent, CD206, confirming the induction of an M2-like phenotype.

Exposures to either SPION formulation induced only slight increases in three of the four pro-inflammatory markers examined (IL-1β, TNFα, and CXCL10), none of which reached statistical significance (adjusted $p > 0.05$). To assess whether these modest changes could be attributed to the dextran coating, we included free carboxymethyl dextran (40 kDa), a polysaccharide derivative commonly used as the shell coating in many dextran-coated SPION formulations [53,54]. The dextran control partially reproduced the increases, particularly for IL-1β and CXCL10, suggesting a potential contribution of the coating to these small

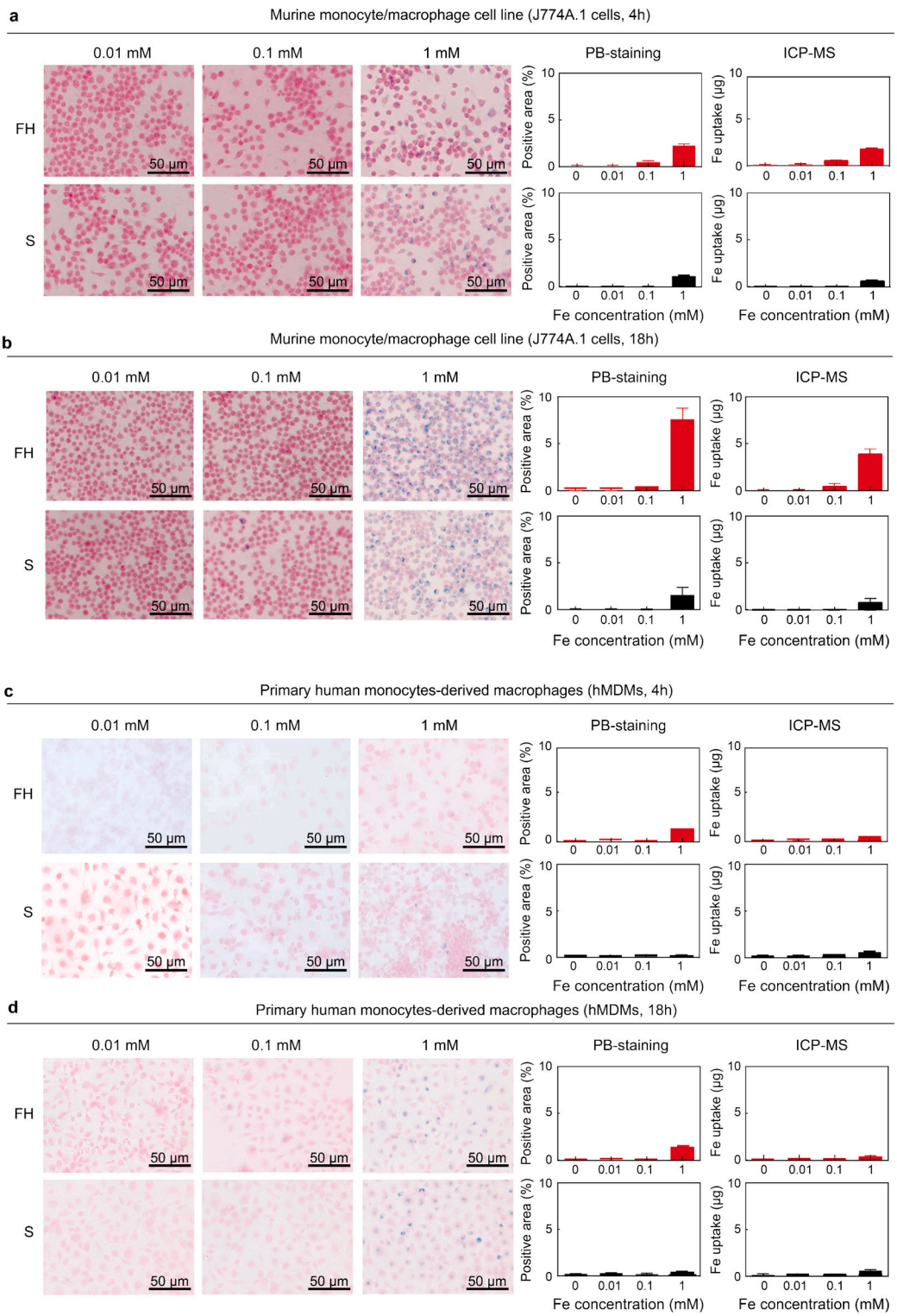


Fig. 2. SPION uptake by macrophages. J774A.1 cells or primary human monocyte-derived macrophages (hMDM) were incubated with Feraheme (FH) or Synomag (S) at 0.01, 0.1, or 1 mM Fe for either 4 h or 18 h. (a) J774A.1, 4 h; (b) J774A.1, 18 h; (c) hMDM, 4 h; (d) hMDM, 18 h, showing Prussian blue bright-field images, Prussian blue–positive area quantified in ImageJ (mean ± SD; $n = 3$), and intracellular iron by ICP-MS (mean ± SD; n = 3). Abbreviations: PB, Prussian blue; ICP-MS, inductively coupled plasma mass spectrometry. (For interpretation of the references to colour in this figure legend, the reader is referred to the web version of this article.)

responses. At 0.1 mM Feraheme, TNFα expression was 5.4-fold higher than in the dextran, although this difference was not statistically significant. Synomag also induced a small increase (2.3-fold) in the anti-inflammatory marker Arg1; however, this was also not statistically significant (adjusted $p > 0.05$). Overall, both SPION formulations induced only minor alterations in gene expression in J774A.1 cells and did not statistically alter polarization-associated gene expression.

Similar gene expression analyses were performed in hMDM (Fig. 3b). For these experiments, the following human-appropriate polarization markers were selected: IL-1β, TNFα, and CXCL10 served as pro-

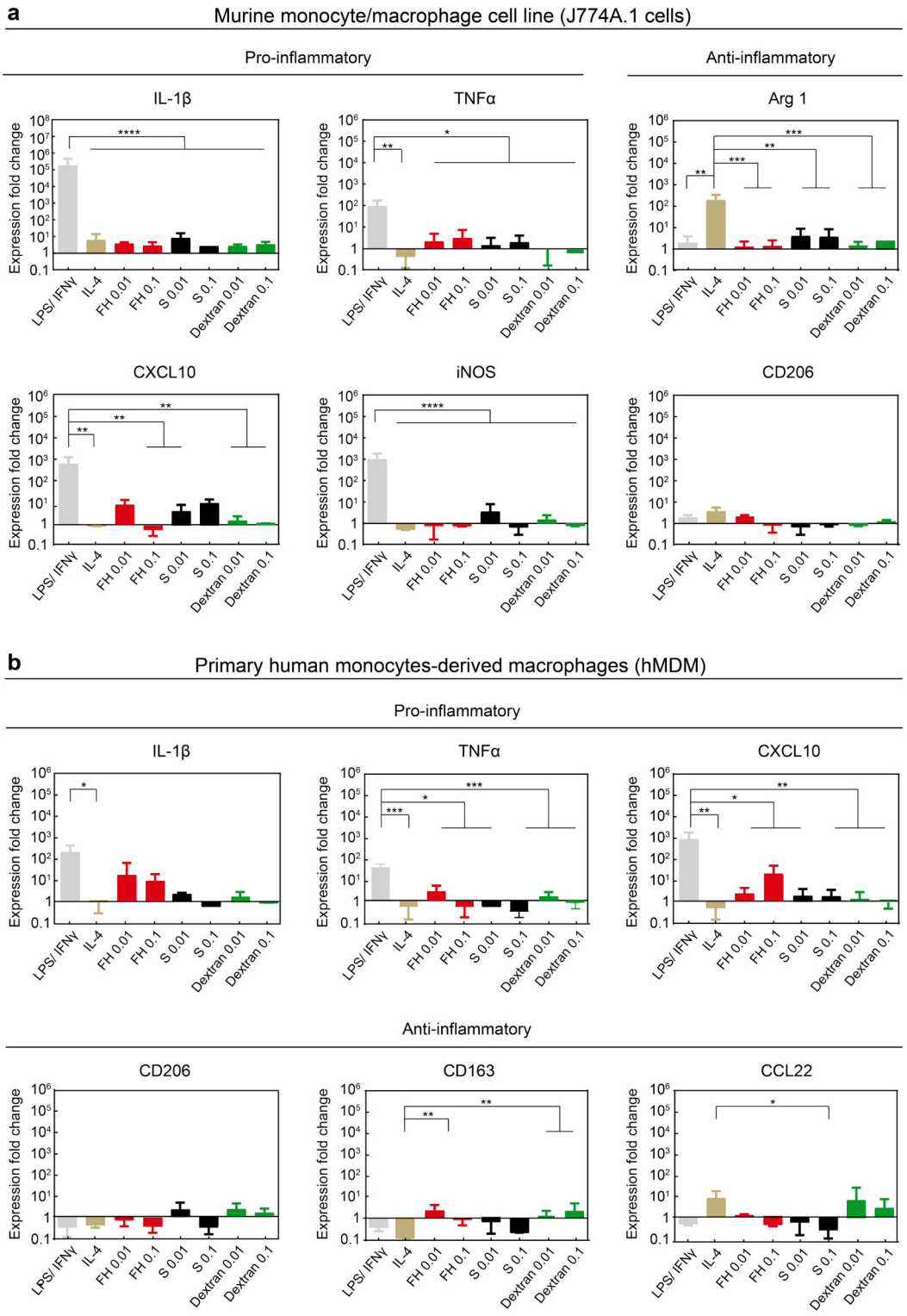


Fig. 3. SPION exposure does not alter macrophage polarization. (a) In J774A.1 cells, the left side shows pro-inflammatory markers (IL-1β, TNFα, CXCL10, iNOS) and the right side shows anti-inflammatory markers (Arg1, CD206). (b) In primary hMDMs, the upper row shows pro-inflammatory markers (IL-1β, TNFα, CXCL10) and the lower row shows anti-inflammatory markers (CD206, CD163, CCL22). Data are displayed as mean ± SD ($n = 3$ per condition). Group differences were assessed using two-way ANOVA on fold-change values (factors: formulation and concentration), followed by Tukey's multiple-comparisons test (family-wise $\alpha = 0.05$). Significance is indicated as (*) $p < 0.05$, (**) $p < 0.01$, and (***) $p < 0.001$ (adjusted p values reported). Only significant pairwise comparisons are marked; unmarked contrasts are not significant.

inflammatory markers, and CD206, CD163, and CCL22 were used as anti-inflammatory ones. This selection reflects well-characterized species differences in macrophage biology: IL-4/STAT6 induces strong Arg1 expression in mouse macrophages [55,56], whereas in human macrophages, Arg1 expression is low and variable. Instead, CD206, CD163, and CCL22 are more reliable indicators of M2-like states in human cells [57–59].

RT-qPCR was also used to assess polarization-related gene expression in the human macrophages, as in similar previous studies [60,61]. After 18 h of exposure to either SPION formulation, hMDM exhibited mostly modest changes in polarization-associated transcripts. Feraheme induced a non-statistically significant trend toward a pro-inflammatory response, with IL-1β, TNFα and CXCL10 expression increasing between 1.5- and 29.1-fold, however, pronounced inter-donor variability and low baseline expression levels of several markers likely contributed to the absence of statistical significance similar to previous reports [62,63]. No consistent pattern was observed for anti-inflammatory markers. Synomag exposure led to a general suppression of both pro- and anti-inflammatory transcripts, with average fold changes ranging from 0.2 to 0.5, although these changes were also not statistically significant. The dextran control also failed to elicit a coherent response, producing only moderate, non-significant upregulation (between 1.3- and 6.9-fold) of the selected anti-inflammatory markers. It is worth noting that intracellular iron levels under these conditions (0.01 and 0.1 mM Fe) were low, particularly in hMDMs. Hence, an additional condition at 1 mM Fe was evaluated in hMDMs (Fig. S1). Under these conditions, CXCL10 showed the clearest trend toward a concentration-dependent increase following Feraheme treatment. In contrast, other pro- and anti-inflammatory markers exhibited only minor or inconsistent changes, and none of these trends reached statistical significance, indicating limited sensitivity of polarization-associated transcripts to SPION dose escalation.

In summary, these *in vitro* studies demonstrated that both Feraheme and Synomag were well tolerated by murine J774A.1 and human hMDM cells, were internalized in a time- and concentration-dependent manner, and produced only non-statistically significant shifts in RNA levels of polarization-associated markers. Because Feraheme is an FDA-approved SPION with established macrophage uptake in patients [64–66], and neither formulation elicited significant transcriptional changes, we selected Feraheme for subsequent *in vivo* evaluation.

3.4. Feraheme treatment does not alter 4 T1 TNBC tumor growth

Excess iron has been reported to exert antitumoral effects through either induction of iron-dependent cell death (ferroptosis) or through macrophage polarization [67,68]. In preclinical models, both ferroptosis and macrophage reprogramming have been implicated in iron-mediated tumor control, although their relative contributions appear to be context-dependent [69–71]. Beyond potential antitumor activity, macrophage polarization has also been linked to vascular function and extracellular matrix remodeling, which could secondarily influence tumor perfusion and the intratumoral delivery of systemically administered nanomedicines [72–74]. Motivated by this evidence, we investigated intravenous Feraheme treatment in a syngeneic, orthotopic 4 T1 TNBC model (Fig. 4a), following its greater *in vitro* internalization and uptake compared to Synomag. Once tumors became palpable (3–4 mm in diameter), mice received six doses (5 mg Fe/kg) of Feraheme on days 7, 9, 11, 13, 15, and 17 post-inoculation. As a result, Feraheme was administered at 30 mg Fe/kg per treatment, a dose within the commonly used range for *in vivo* SPION studies [75–77]. Moreover, using body-surface-area (Km) scaling (Km_mouse = 3; Km_human = 37), this dose corresponds to a human-equivalent dose of 2.4 mg/kg, which is close to

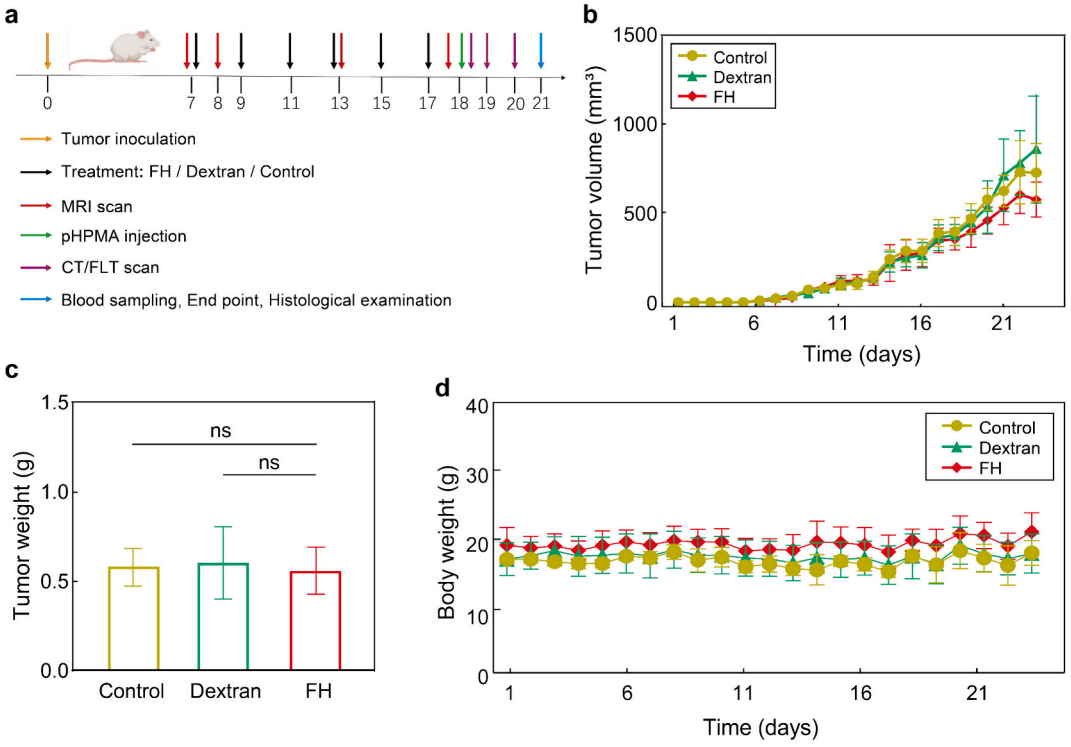


Fig. 4. Feraheme treatment does not affect 4 T1 TNBC tumor growth. (a) Immunocompetent female BALB/c mice were orthotopically inoculated with 2.5×10^4 4 T1 triple-negative breast cancer cells. After tumors were palpable (*i.e.* 3–4 mm in diameter, day 7), Feraheme was intravenously administered every two days for a total of six injections (5 mg Fe/kg per injection, 30 mg Fe/kg in total); PBS and dextran were used as controls. (b) Tumor volume over time based on caliper measurements. (c) *Ex vivo* tumor weight on day 21. (d) Mouse body weight was recorded longitudinally during treatment. Data are displayed as mean ± SD; ns = not significant (adjusted $p > 0.05$). Abbreviations: MRI, magnetic resonance imaging; pHPMA, poly(*N*-(2-hydroxypropyl)methacrylamide); CT/FLT, computed tomography/fluorescence lifetime imaging.

the 3 mg/kg Feraheme imaging dose and consistent with typical clinical practice ranges (1–5 mg/kg) [78–80].

Two additional control groups were included: a standard saline control group, and a dextran control group consisting of free carboxymethyl dextran (40 kDa) in solution. The latter was included to account for potential effects associated with the polysaccharide coating material itself, independent of the iron oxide core [81,82]. This study design allowed us to disentangle SPION-specific effects from those arising from particle coating itself or from baseline physiology.

Tumor volumes were monitored over the course of the study and did not differ significantly between groups, reaching 559 ± 98 mm^3 (Feraheme), 753 ± 206 mm^3 (Dextran), and 661 ± 94 mm^3 (Control) after three weeks ($p > 0.05$ for all; Fig. 4b). *Ex vivo* tumor weights at day 21 confirmed these findings (Fig. 4c). No group exhibited significant weight loss, indicating good tolerability of the treatments (Fig. 4d).

3.5. Feraheme treatment strongly increases iron levels in 4 T1 TNBC tumors

To exert physiological effects, SPION must effectively reach the pathological site. However, TNBC tumors, such as 4 T1, typically exhibit a dense TME and highly abnormal vasculature, both of which hinder efficient nanomedicine delivery [83,84]. Therefore, we evaluated Feraheme accumulation in tumors using *in vivo* MR imaging, histopathology, and mass spectrometry. For longitudinal imaging, animals underwent a baseline (pre-treatment) MRI followed by serial scans during the treatment course. Qualitative T_2-weighted images were used to localize orthotopic tumors, whereas quantitative T_2* mapping enabled temporal monitoring of iron deposition. As shown in Fig. 5a, tumors from Feraheme-treated mice displayed pronounced hypointense regions, consistent with iron accumulation. Quantification by T_2* relaxation times on days 1, 6, and 11 after the initial administration

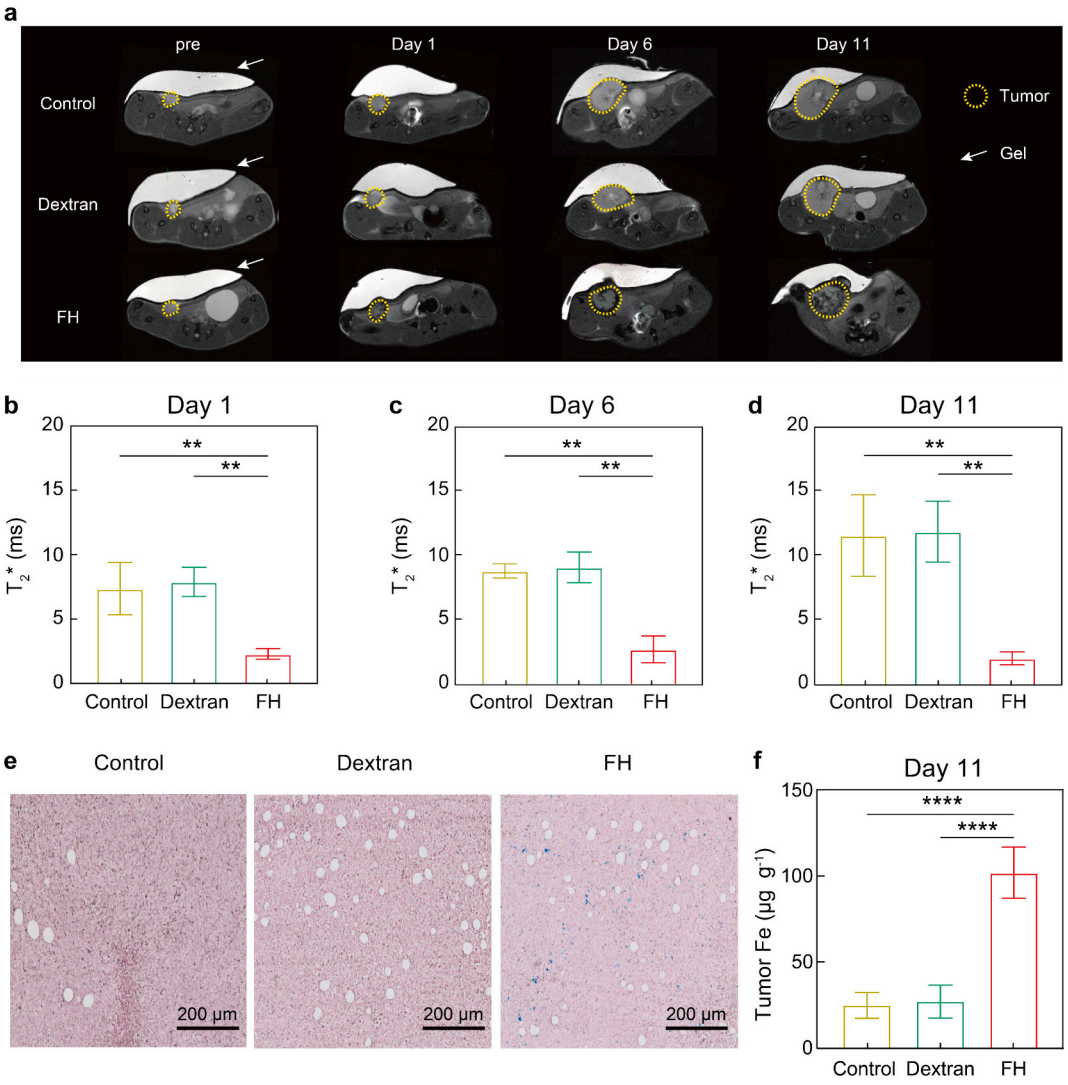


Fig. 5. Feraheme treatment elevates tumor iron levels. (a) T_2-weighted MRI (pre-treatment baseline and during treatment) shows marked darkening of orthotopic tumors over time in Feraheme-treated mice; tumors are indicated with yellow dashed outlines. Note that ultrasound gel (bright white) was applied outside the tumors to reduce artifacts in the T_2-weighted images. T_2* relaxation times were acquired longitudinally at (b) day 1, (c) day 6, and (d) day 11 after treatment initiation. (e) Bright-field microscopy of Prussian blue-stained tumor tissue shows iron accumulation in the Feraheme-treated group. (f) ICP-MS quantification shows a significant increase in tumor iron levels in the Feraheme-treated group at day 11. Data are displayed as mean ± SD. Significance is indicated as (**) $p < 0.01$ and (****) $p < 0.0001$ (adjusted p values reported). (For interpretation of the references to colour in this figure legend, the reader is referred to the web version of this article.)

(Figs. 5b-d) corroborated these visual observations. In contrast, tumors in the control and dextran groups maintained higher signal intensities (up to 3.6-fold higher than in the Feraheme group) throughout the course of the study, indicative of low iron deposition.

Histological analysis corroborated these results: Prussian blue staining revealed markedly increased iron levels in tumor sections from Feraheme-treated animals (Fig. 5e). To complement the imaging and histology data, *ex vivo* ICP-MS analysis was performed on day 11 and showed an over 4-fold increase in tumor iron content in the Feraheme group compared to the control and dextran groups (Fig. 5f). ICP-MS confirmed elevated iron levels in the liver and spleen of Feraheme-treated mice, consistent with SPION accumulation in the mononuclear phagocyte system (Fig. S2). Collectively, these results show substantial tumor-associated iron accumulation following intravenous Feraheme administration.

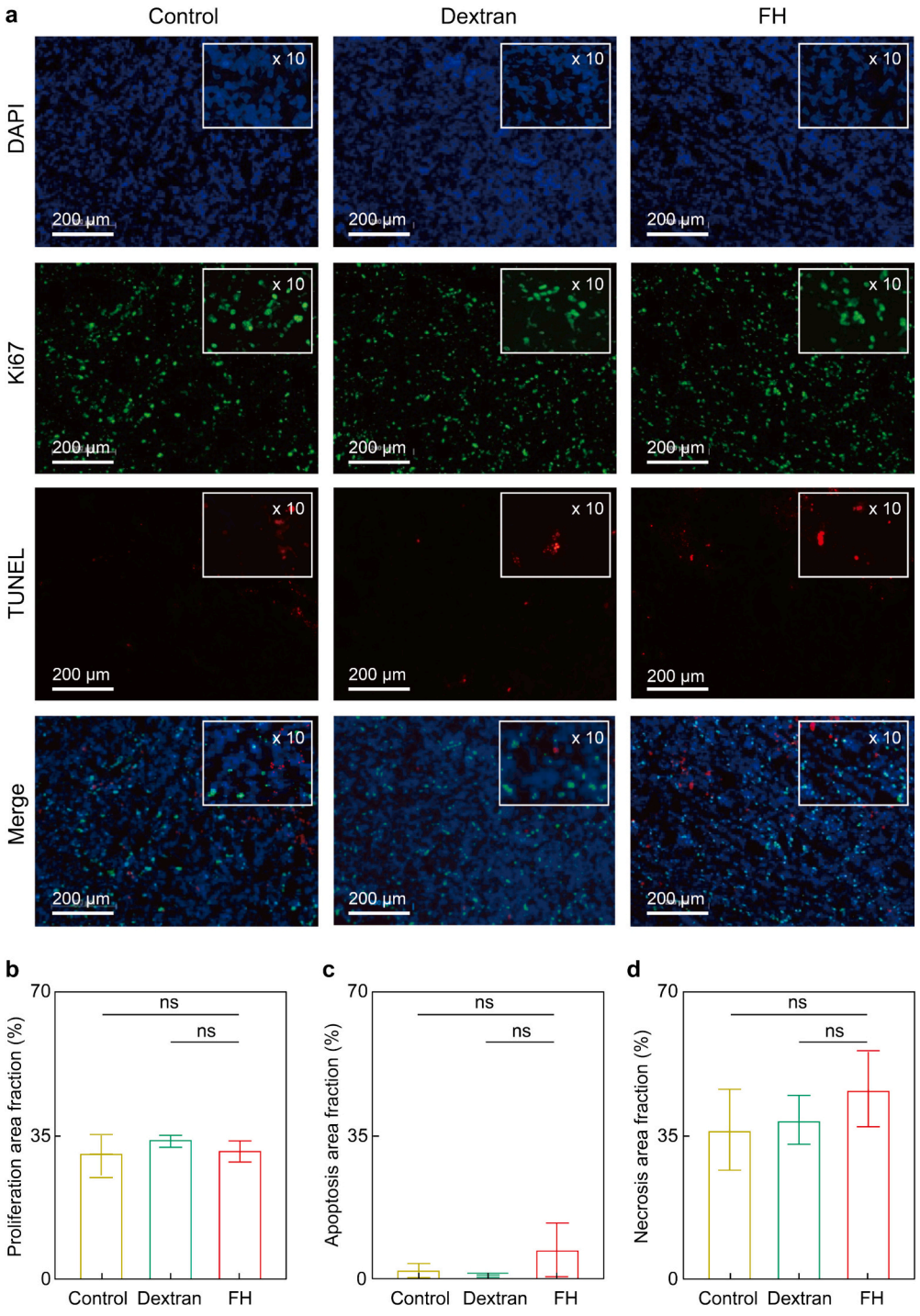


Fig. 6. Feraheme treatment does not affect proliferation, apoptosis and necrosis in 4 T1 tumors. (a) Histological micrographs of tumor sections showing DAPI (nuclei, blue), Ki67 (proliferation, green), and TUNEL (apoptosis, red); Merge shows the overlay of the three channels. Insets show 10× magnifications. Quantification of (b) Ki67 (proliferation), (c) TUNEL (apoptosis), and (d) necrotic area in H&E staining, showing no significant differences between the treatments. Representative H&E images are provided in Fig. S3. Data are displayed as mean ± SD; ns = not significant (adjusted $p > 0.05$). (For interpretation of the references to colour in this figure legend, the reader is referred to the web version of this article.)

3.6. Feraheme treatment does not affect 4 T1 TNBC proliferation, apoptosis, and necrosis

Having established that upon intravenous administration, Feraheme successfully reaches 4 T1 tumors yet does not affect their macroscopic growth, we next explored whether the iron oxide nanoparticles elicit detectable biological effects. Histological analyses were performed to assess tumor-cell proliferation (Ki67), apoptosis (TUNEL), and necrosis (H&E), with DAPI used for nuclear counterstaining in immunofluorescence (Fig. 6a). Quantification was performed as area fraction (% of the total tumor area) for each marker, based on three sections per mouse.

Across the control, dextran, and Feraheme groups, no significant differences in proliferative activity were observed (Fig. 6b). Tumors treated with Feraheme showed a trend toward increased apoptosis and necrosis compared with controls (Fig. 6b-d), but these differences did not reach statistical significance ($p > 0.05$). These findings suggest that Feraheme may exert moderate effects, which are likely obscured by underlying biological variability.

3.7. Feraheme treatment does not affect the tumor immune microenvironment

Given that Feraheme did not alter tumor-cell proliferation or induce significant cell death, we next examined whether the accumulated nanoparticles affected macrophage density or polarization in the tumor, liver, and spleen. After sacrifice, tumors and organs were harvested, immune cells were isolated, and populations were analyzed by flow cytometry (gating strategy shown in Fig. S4a). Briefly, live singlets negative for 7-AAD were selected and gated on $CD45^+$ leukocytes. Within this compartment, $CD11b^+$ myeloid cells were identified, and $F4/80^+$ macrophages were quantified. Macrophage polarization was then evaluated within the $F4/80^+$ population by assessing MHC class II (MHCII) and CD206 expression as markers of pro- and anti-inflammatory phenotypes, respectively.

In tumors, Feraheme, dextran, and control groups showed no significant differences in total macrophage abundance or MHCII/CD206 expression profiles (Fig. 7a-d). In the liver, Feraheme treatment induced a modest yet significant increase in total $F4/80^+$ macrophages, whereas the proportions of $MHCII^+$ (M1-like) and $CD206^+$ (M2-like) subsets remained unchanged, indicating no detectable polarization shift (Fig. S4b). In the spleen, neither total macrophage numbers nor polarization markers differed among groups (Fig. S4c).

Nanomedicines can also modulate other immune compartments within the tumor microenvironment. We therefore analyzed several T-cell subsets across the three treatment groups (gating strategy shown in Fig. S5a). Briefly, $CD45^+$ leukocytes were identified and gated for $CD3^+$ T cells, which were subsequently subdivided into $CD4^+$ helper and $CD8^+$ cytotoxic T-cells populations. As shown in Fig. 7e-h and Figs. S5a-5b, no significant differences were detected in any T-cell population in tumors, liver, or spleen.

3.8. Effect of Feraheme treatment on tumor-targeted drug delivery

Lastly, we explored whether Feraheme pre-treatment could enhance

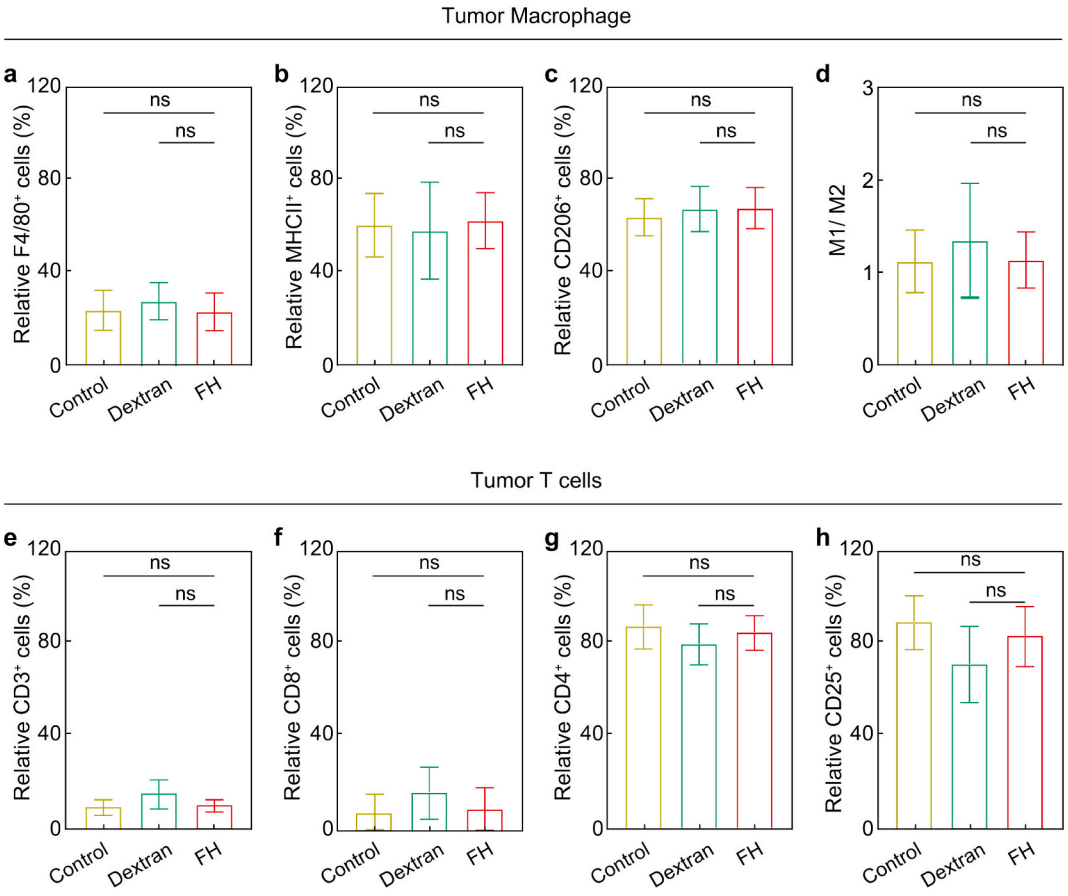


Fig. 7. Feraheme treatment does not alter the tumor microenvironment. Tumors were analyzed by flow cytometry after treatment. (a) Quantification of tumor-associated macrophages ($F4/80^+$) shows no significant differences between the treatment groups. (b–d) Macrophage phenotypes within $F4/80^+$ cells: (b) $MHCII^+$ (pro-inflammatory/M1-like) and (c–d) $CD206^+$ (anti-inflammatory/M2-like) subpopulations, showing no changes upon Feraheme treatment. (e) Total T cells ($CD3^+$) and (f) $CD8^+$ cytotoxic, (g) $CD4^+$ helper, and (h) $CD25^+$ activated helper T cells. No significant differences were observed between the treatment groups. Data are displayed as mean ± SD; ns = not significant (adjusted $p > 0.05$).

the tumor-directed delivery of nanomedicines. We used Cy7-labeled pHPMA (10 nm) as a prototypic nanocarrier, given its good *in vivo* performance and extensive use in previous studies [85,86]. pHPMA was intravenously administered after the sixth Feraheme (dextran or saline) dose, and its biodistribution was monitored by CT-FLT imaging at 0.25, 4, 24, 48, and 72 h (Fig. 8a). Tumor accumulation, expressed as percentage injected dose (% ID/g), increased over time and reached approximately 1–4% after 48 h (Fig. 8b). Although the FMT-reconstructed images (Fig. 8a) exhibited bright fluorescence signals in the vicinity of pathological tissue, careful tumor segmentation based on co-registered CT data allowed exclusion of signal spillover and artifacts originating from adjacent organs. Consequently, the quantified tumor accumulation values remained below 5% ID/g and are consistent with previously reported uptake profiles for the same nanopolymer at

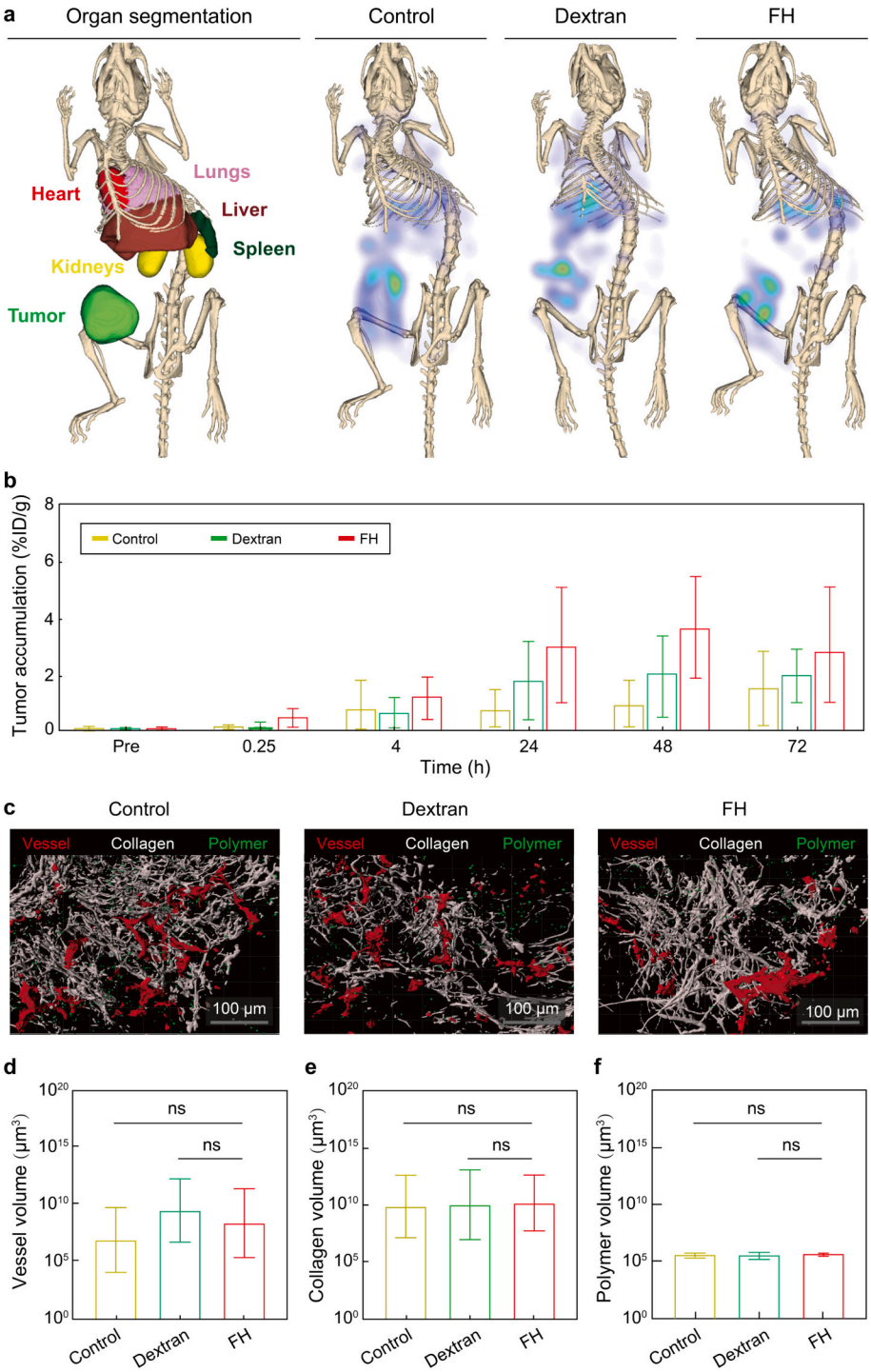


Fig. 8. Feraheme pre-treatment does not alter polymeric nanocarrier delivery nor the TME. (a) Hybrid CT-FLT imaging at 0.25, 4, 24, 48, and 72 h was used to track the *in vivo* biodistribution of Cy7-labeled pHPMA. (b) Quantification of tumor accumulation of Cy7-labeled pHPMA in Feraheme-, dextran-, and PBS-pre-treated mice, expressed as percent injected dose (% ID), showing no significant differences. (c) Representative TPLSM images of orthotopic 4 T1 tumors showing lectin-positive perfused blood vessels (red), collagen fibers visualized by second-harmonic generation (gray), and polymer signal (green). (d) Quantification of total lectin (vessel) volume. (e) Quantification of collagen volume. (f) Quantification of intratumoral polymer content. Data are displayed as mean ± SD; ns = not significant (adjusted $p > 0.05$). (For interpretation of the references to colour in this figure legend, the reader is referred to the web version of this article.)

comparable time points [87]. All groups exhibited progressively elevated liver signal post-injection (up to 23% ID/g), whereas uptake in other organs was small and decreased over time (Fig. S6), consistent with the known behavior of similar nanocarriers [88–90]. Although the Feraheme-pretreated group showed higher pHPMA tumor accumulation after 24 h than the dextran- and saline-treated control groups, with increases ranging from 1.6- to 2.7-fold, these differences did not reach statistical significance ($p > 0.05$). This non-significant increase is consistent with the results of the previous section, where SPION treatments appeared to induce biological effects that were modest and did not reach statistical significance, likely due to their small magnitude relative to biological heterogeneity. Similarly, the Feraheme-treated group showed a trend toward reduced hepatic pHPMA uptake compared with the other two groups; however, this difference was also not statistically significant.

To further validate these results, and to confirm that Feraheme pretreatment did not induce meaningful changes in either nanomedicine delivery or in the tumor microenvironment, we harvested, sectioned, and analyzed 4 T1 tumors by TPLSM 72 h after pHPMA administration. Collagen fibers were visualized *via* second-harmonic generation, and blood vessels were labeled with intravenously injected rhodamine-lectin. Tumor vasculature and collagen were jointly imaged using second-harmonic generation / fluorescence imaging (collagen in gray, vessels in red, polymer in green). As shown in Fig. 8c, lectin-positive vessel volume per field of view and collagen density appeared qualitatively similar across groups. Quantification of vessel density (Fig. 8d), collagen content (Fig. 8e), and polymer content (Fig. 8f) revealed no statistically significant differences. Collectively, these results corroborate that Feraheme priming does not alter TME nor the tumor accumulation of nanomedicine formulations.

4. Discussion

Our results demonstrate that Feraheme exhibits a high-accumulation, low-interference profile in established 4 T1 TNBC tumors. Under the dosing and timing used here, Feraheme neither exerted direct antitumor effects nor caused statistically significant alterations in the TME, supporting its role as an imaging agent for TAM visualization and quantification, rather than as a therapeutic agent. Consistent with our findings, a study using a dual-tumor 4 T1 mammary cancer mouse model found that Feraheme (40 mg/kg) did not repolarize TAMs toward an M1-like phenotype, despite clear Feraheme uptake detectable by MRI [91]. Moreover, a study using an aggressive syngeneic TNBC model reported robust Feraheme phagocytosis by intratumoral TAMs and demonstrated quantitative “iron-mapping” MRI as a surrogate for TAM density over time, supporting Feraheme as a high-accumulation tracer for TAM visualization rather than a consistent immunomodulatory primer [92]. Consistent with this, Feraheme pre-treatment did not enhance the delivery of a prototypic polymeric nanocarrier. Taken together, these observations may help explain why Feraheme pretreatment in our study produced a modest and not statistically significant enhancement in the delivery of a prototypic polymeric nanocarrier. Feraheme appeared to elicit some biological changes, in some specific markers, that did not reach statistical significance, likely because their magnitude was small compared to the underlying biological variability.

In our study, macrophage polarization *in vivo* was assessed using MHCII and CD206, two biomarkers commonly used for M1-like and M2-like polarization assessment. However, M1 *vs* M2 is a simplified polarization framework, which is not strict binary. In reality, macrophages exist on a spectrum of activated states. Hence, our approach, while valid to characterize traditional M1 *vs* M2 polarization, can limit the resolution for detecting more subtle or iron-associated macrophage state changes. Accordingly, future studies employing broader phenotyping panels, including additional M1-associated co-stimulatory markers such as CD86 could further improve the characterization of macrophage activation states. Similarly, T-cell phenotyping was restricted to $CD3^+$, $CD4^+$, and $CD8^+$ subsets, without assessment of activation markers or regulatory T cells (Tregs; CD25/FoxP3); their inclusion in future studies could help resolve more subtle immunomodulatory effects. In addition, high-dimensional profiling approaches such as scRNA-seq of sorted $F4/80^+$ cells could provide an unbiased view of macrophage state changes that may be missed by marker-based phenotyping [93–95].

Moreover, this study did not aim to directly map how intratumoral SPION-associated iron is distributed across distinct cellular or subcellular compartments, nor quantify SPION uptake in a cell-type-resolved manner across TAMs, tumor cells, endothelial cells, and other stromal or immune compartments, as partially performed in other reports [96–98], but thus far not explored in the context of enhanced drug delivery and improved targeted therapy. We acknowledge that the bulk tumor iron loading does not necessarily reflect increased bioavailable iron at the cellular level, hence, iron may remain sequestered within nanoparticle cores and/or lysosomal compartments [95,99–101]. Future studies should aim to combine flow-sorted iron quantification with high-resolution co-localization imaging and ferroptosis-focused assays yielding insights on whether iron bioavailability and iron-dependent cell-death pathways contribute to the observed phenotype [102–104].

Our findings differ from previous studies reporting that under certain circumstances, (ligand-functionalized) SPION can modulate several aspects on tumor growth and TME composition. For example, β-glucan-coupled SPION have been shown to induce macrophage-trained immunity *via* mTOR-dependent pathways and improve survival in infection models [105]. Another study demonstrated that clinically used SPION can activate TLR4 signaling, promoting macrophage autophagy and inflammatory responses both *in vitro* and *in vivo* [106]. In addition, a study using a murine mammary adenocarcinoma model found that Feraheme, administered either at tumor cell implantation or as a pretreatment prior to intravenous tumor cell injection, inhibited primary tumor growth and reduced metastasis *via* pro-inflammatory macrophage polarization, increased ROS, and caspase-3-associated tumor-cell apoptosis [11].

In contrast, upon applying our regimen in established syngeneic and orthotopic 4 T1 TNBC tumors, clinically used Feraheme generated substantially increased amounts of intratumoral iron levels, but this came with minimal perturbation of the TME, tumor growth and tumor-targeted nanomedicine delivery. These discrepancies likely arise from differences in ligand functionalization, disease context, tumor stage, and/or dosing/timing across studies. These distinctions support our conclusion that, in this setting, Feraheme primarily serves as a high-accumulation, low-interference imaging agent to capture TAM levels, rather than as an antitumor or TME-priming agent. This may, however, vary with tumor type, nanoparticle concentration, and SPION type. In addition, as the 4 T1 model is generally considered an immunologically “cold” tumor, the magnitude and threshold of SPION-driven immunomodulation may differ in immunologically “hot” models such as CT26 or MC38 [107–109]. Looking ahead, achieving robust TAM reprogramming may require SPION designs that extend beyond iron delivery and incorporate immunologically active surface features engaging innate immune pathways. Indeed, engineered SPION formulations with macrophage-responsive surface designs have been shown to induce substantially stronger pro-inflammatory activation than plain SPION [48,71]. Moreover, combination strategies such as vascular normalization with anti-angiogenic co-treatment may improve the uniformity of intratumoral SPION distribution and thereby increase the likelihood of functional immune modulation [110,111]. In addition, combination regimens such as magnetic hyperthermia could be explored to provide immunogenic stress cues and thereby facilitate functional TME remodeling [112–114]. Furthermore, intervention timing in early *versus* established tumors and dose density may influence whether SPION-mediated effects become detectable, and this issue remains to be systematically addressed in future studies, ideally together with expanded TAM phenotyping [115–118].

Overall, these collective observations support the concept of repurposing Feraheme as a companion nanodiagnostic, rather than as a standalone therapeutic agent [119]. Although more than twenty classical anticancer nanomedicines are nowadays used in the clinic [10,120], tumor accumulation is highly variable across and within patients, underscoring the need for predictive biomarkers [119]. Supporting this idea, an early clinical study has shown that higher pre-therapy Feraheme uptake on MRI correlates with greater tumor shrinkage and higher intratumoral levels of liposomal irinotecan (Onivyde), illustrating how SPION can serve as imageable surrogates for nanomedicine accumulation, likely *via* TAM capture, and how they can thus aid in patient selection [121]. Collectively, the results presented here indicate that the effect of targeted iron overload in tumors and TAM is highly context-dependent. In our study, Feraheme efficiently accumulated in 4 T1 tumors without noticeable antitumor effects and TME remodeling, making them valuable as diagnostic tracers for assessing tumor accumulation and potentially guiding patient selection, but not as priming agents to improve the delivery and/or efficacy of subsequently administered (nano)drugs.

5. Conclusion

In this study, we evaluated if commercially available SPION formulations can change the polarization of TAM, modulate the TME, affect tumor growth, and influence tumor-targeted drug delivery. Feraheme and Synomag were efficiently internalized by macrophages *in vitro* but induced only modest changes in polarization markers. *In vivo*, repeated intravenous administrations of Feraheme in mice bearing syngeneic and orthotopic 4 T1 tumors were well tolerated and resulted in substantial intratumoral iron accumulation without affecting tumor growth, proliferation, apoptosis, necrosis, and the abundance and polarization of TAM and T-cell populations. Likewise, Feraheme pre-treatment did not enhance the delivery of a model polymeric nanocarrier. Overall, Feraheme displayed a high-accumulation, low-interference profile, loading tumors with iron but not measurably remodeling the TME or improving antitumor efficacy or nanodrug delivery. These findings support the use of SPION as imageable tracers and companion diagnostics for assessing TAM levels and nanomedicine tumor accumulation, rather than as antitumor therapeutic and TME-priming agents. Importantly, this notion is based only on the orthotopic 4 T1 TNBC model, on the specific SPION formulations tested, and on the dosing regimen applied in this study. Future efforts should therefore include a broader range of SPION specimens and dosing regimens across multiple tumor types, in order to able to further generalize these observations.

CRediT authorship contribution statement

Karolin Roemhild: Writing – review & editing, Writing – original draft, Investigation, Formal analysis, Data curation, Conceptualization. **Yanchen Li:** Writing – review & editing, Writing – original draft, Visualization, Methodology, Formal analysis, Data curation. **Roman A. Barmin:** Writing – original draft, Project administration, Methodology, Formal analysis, Data curation. **Seyed Mohammadali Dadfar:** Writing – review & editing, Writing – original draft, Methodology, Investigation, Formal analysis, Data curation. **Ekaterina Savina:** Writing – review & editing, Methodology, Investigation, Formal analysis, Conceptualization. **Kim Lindelauf:** Writing – review & editing, Methodology, Investigation, Formal analysis. **Diana Moeckel:** Writing – review & editing, Methodology, Investigation, Formal analysis. **Elena Rama:** Writing – review & editing, Methodology, Funding acquisition, Formal analysis. **Teresa Lemainque:** Writing – review & editing, Methodology, Investigation. **Finn von Maltzahn:** Writing – review & editing, Methodology, Formal analysis. **Sven Thoröe-Boveleth:** Writing – review & editing, Methodology, Data curation. **Robert Pola:** Writing – review & editing, Resources, Methodology. **Tomas Etrych:** Writing – review & editing, Resources, Methodology. **Ruth Knuechel-Clarke:** Writing – review & editing, Supervision, Project administration, Funding acquisition. **Peter Boor:** Writing – review & editing, Visualization, Validation, Formal analysis. **Thomas Kraus:** Writing – review & editing, Resources, Methodology. **Volkmar Schulz:** Writing – review & editing, Visualization, Methodology. **Jan Grimm:** Writing – review & editing, Supervision, Methodology, Investigation. **Fabian Kiessling:** Writing – review & editing, Supervision, Project administration, Funding acquisition. **Saskia von Stillfried:** Writing – review & editing, Methodology, Investigation, Funding acquisition. **Roger M. Pallares:** Writing – review & editing, Visualization, Project administration, Data curation. **Twan Lammers:** Writing – review & editing, Supervision, Project administration, Methodology, Funding acquisition, Conceptualization.

Data availability

Data will be made available on request.

Acknowledgments

This work was funded by the German Research Foundation (DFG: GRK 2375 (grant #331065168)), the European Research Council (ERC CoG 864121, Meta-Targeting), and the Federal Ministry of Education and Research (BMBF) and the Ministry of Culture and Science of the German State of North Rhine-Westphalia (MKW) under the Excellence Strategy of the Federal Government and the Länder through the Junior Principal Investigator Fellowship. This work was supported in part by the National Institutes of Health (NIH) R01CA218615, R01CA215700, R01EB033000 (to JG) and P30 CA08748. The experimental part was supported by the Flow Cytometry core facility of the Interdisciplinary Center for Clinical Research (IZKF) within the Faculty of Medicine at RWTH Aachen University.

Appendix A. Supplementary data

Supplementary data to this article can be found online at https://doi.org/10.1016/j.jconrel.2026.114726.

References

[1] S.M. Dadfar, K. Roemhild, N.I. Drude, S. von Stillfried, R. Knüchel, F. Kiessling, T. Lammers, Iron oxide nanoparticles: diagnostic, therapeutic and theranostic applications, Adv. Drug Deliv. Rev. 138 (2019) 302–325.
[2] M.G. Harisinghani, J. Barentsz, P.F. Hahn, W.M. Deserno, S. Tabatabaei, C. H.v. d Kaa, J.d.l. Rosette, R. Weissleder, Noninvasive detection of clinically occult lymph-node metastases in prostate Cancer, N. Engl. J. Med. 348 (25) (2003) 2491–2499.
[3] K.-L. Nguyen, T. Yoshida, N. Kathuria-Prakash, I.H. Zaki, C.G. Varallyay, S. I. Semple, R. Saouaf, C.K. Rigsby, S. Stoumpos, K.K. Whitehead, L.M. Griffin, D. Saloner, M.D. Hope, M.R. Prince, M.A. Fogel, M.L. Schiebler, G.H. Roditi, A. Radjenovic, D.E. Newby, E.A. Neuwelt, M.R. Bashir, P. Hu, J.P. Finn, Multicenter safety and practice for off-label diagnostic use of Ferumoxytol in MRI, Radiology 293 (3) (2019) 554–564.
[4] Y. Li, R. Barmin, R. Zhang, F. Kiessling, T. Lammers, R.M. Pallares, Clinical translation and landscape of superparamagnetic iron oxide nanoparticles, Adv. Drug Deliv. Rev. 229 (2026) 115756.
[5] F.M.E. Segers, A.V. Ruder, M.M. Westra, T. Lammers, S.M. Dadfar, K. Roemhild, T.S. Lam, M.E. Kooi, K.B.J.M. Cleutjens, F.K. Verheyen, G.W.H. Schurink, G. R. Haenen, T.J.C. van Berkel, I. Bot, B. Halvorsen, J.C. Sluimer, E.A.L. Biessen, Magnetic resonance imaging contrast-enhancement with superparamagnetic iron oxide nanoparticles amplifies macrophage foam cell apoptosis in human and murine atherosclerosis, Cardiovasc. Res. 118 (17) (2022) 3346–3359.
[6] K. Roemhild, F. von Maltzahn, R. Weiskirchen, R. Knüchel, S. von Stillfried, T. Lammers, Iron metabolism: pathophysiology and pharmacology, Trends Pharmacol. Sci. 42 (8) (2021) 640–656.
[7] S.M. Dadfar, D. Camozzi, M. Darguzyte, K. Roemhild, P. Varvara, J. Metselaar, S. Banala, M. Straub, N. Guvener, U. Engelmann, I. Slabu, M. Buhl, J. van Leusen, P. Kogerler, B. Hermanns-Sachweh, V. Schulz, F. Kiessling, T. Lammers, Size-isolation of superparamagnetic iron oxide nanoparticles improves MRI, MPI and hyperthermia performance, J. Nanobiotechnol. 18 (1) (2020) 22.
[8] M.H. Schwenk, Ferumoxytol: a new intravenous iron preparation for the treatment of iron deficiency anemia in patients with chronic kidney disease, Pharmacotherapy 30 (1) (2010) 70–79.
[9] Y. Li, R. Zhang, R. Barmin, E. Rama, M. Schoenen, F. Schrank, V. Schulz, I. Slabu, F. Kiessling, T. Lammers, R.M. Pallares, Improving MPI and hyperthermia

performance of superparamagnetic iron oxide nanoparticles through fractional factorial design of experiments, Nanoscale Adv. 6 (17) (2024) 4352–4359.
[10] R.M. Pallares, R.A. Barmin, A. Wang, F. Kiessling, T. Lammers, Clinical cancer nanomedicines, J. Control. Release 385 (2025) 113991.
[11] S. Zanganeh, G. Hutter, R. Spitler, O. Lenkov, M. Mahmoudi, A. Shaw, J. S. Pajarinen, H. Nejadnik, S. Goodman, M. Moseley, L.M. Coussens, H.E. Daldrup-Link, Iron oxide nanoparticles inhibit tumour growth by inducing pro-inflammatory macrophage polarization in tumour tissues, Nat. Nanotechnol. 11 (11) (2016) 986–994.
[12] H.E. Daldrup-Link, D. Golovko, B. Ruffell, D.G. DeNardo, R. Castaneda, C. Ansari, J. Rao, G.A. Tikhomirov, M.F. Wendland, C. Corot, L.M. Coussens, MRI of tumor-associated macrophages with clinically applicable Iron oxide nanoparticles, Clin. Cancer Res. 17 (17) (2011) 5695–5704.
[13] A. Christofides, L. Strauss, A. Yeo, C. Cao, A. Charest, V.A. Boussiotis, The complex role of tumor-infiltrating macrophages, Nat. Immunol. 23 (8) (2022) 1148–1156.
[14] Z. Bian, Y. Gong, T. Huang, C.Z.W. Lee, L. Bian, Z. Bai, H. Shi, Y. Zeng, C. Liu, J. He, J. Zhou, X. Li, Z. Li, Y. Ni, C. Ma, L. Cui, R. Zhang, J.K.Y. Chan, L.G. Ng, Y. Lan, F. Ginhoux, B. Liu, Deciphering human macrophage development at single-cell resolution, Nature 582 (7813) (2020) 571–576.
[15] D.G. DeNardo, B. Ruffell, Macrophages as regulators of tumour immunity and immunotherapy, Nat. Rev. Immunol. 19 (6) (2019) 369–382.
[16] S.K. Biswas, M. Chittezhath, I.N. Shalova, J.-Y. Lim, Macrophage polarization and plasticity in health and disease, Immunol. Res. 53 (1) (2012) 11–24.
[17] P.J. Murray, Macrophage polarization, Annu. Rev. Physiol. 79 (2017) 541–566.
[18] H. Jeong, I. Hwang, S.H. Kang, H.C. Shin, S.Y. Kwon, Tumor-associated macrophages as potential prognostic biomarkers of invasive breast Cancer, J. Breast Cancer 22 (1) (2019) 38–51.
[19] A. Mantovani, P. Allavena, F. Marchesi, C. Garlanda, Macrophages as tools and targets in cancer therapy, Nat. Rev. Drug Discov. 21 (11) (2022) 799–820.
[20] T. Ojha, G.J.L. Schaefer, R. Mihyar, V. Pathak, J. Ehling, E. Rama, F. De Lorenzi, A.S. Elshafei, D. Moeckel, S. Elsafy, B. Theek, M. Wagner, P. Ceccarini, L. Consolino, M. Weiler, F. Peisker, T. Caspers, Q. Peña, R. Barmin, F. Gremse, R. Pola, M. Pechar, T. Etrych, S. Meurer, R. Weiskirchen, R. Kramann, F. Kiessling, G. Storm, J. Metselaar, T. Lammers, Desmoplastic tumor priming using clinical-stage corticosteroid liposomes, Cell Biomater. 1 (3) (2025).
[21] R.M. Pallares, F.M. Mottaghy, V. Schulz, F. Kiessling, T. Lammers, Nanoparticle diagnostics and Theranostics in the clinic, J. Nucl. Med. 63 (12) (2022) 1802–1808.
[22] I.V. Zelepukin, K.G. Shevchenko, S.M. Deyev, Rediscovery of mononuclear phagocyte system blockade for nanoparticle drug delivery, Nat. Commun. 15 (1) (2024) 4366.
[23] T. Ganz, Macrophages and Iron metabolism, Microbiol. Spectr. 4 (5) (2016).
[24] G. Cairo, S. Recalcati, A. Mantovani, M. Locati, Iron trafficking and metabolism in macrophages: contribution to the polarized phenotype, Trends Immunol. 32 (6) (2011) 241–247.
[25] F. Vinchi, M. Costa da Silva, G. Ingoglia, S. Petrillo, N. Brinkman, A. Zuercher, A. Cerwenka, E. Tolosano, M.U. Muckenthaler, Hemopexin therapy reverts heme-induced proinflammatory phenotypic switching of macrophages in a mouse model of sickle cell disease, Blood 127 (4) (2016) 473–486.
[26] M. Costa da Silva, M.O. Breckwoldt, F. Vinchi, M.P. Correia, A. Stojanovic, C. M. Thielmann, M. Meister, T. Muley, A. Warth, M. Platten, M.W. Hentze, A. Cerwenka, M.U. Muckenthaler, Iron induces anti-tumor activity in tumor-associated macrophages, Front. Immunol. 8 (2017).
[27] T.A. Bauer, N.K. Horvat, O. Marques, S. Chocarro, C. Mertens, S. Colucci, S. Schmitt, L.M. Carrella, S. Morsbach, K. Koynov, F. Fenaroli, P. Blümler, M. Jung, R. Sotillo, M.W. Hentze, M.U. Muckenthaler, M. Barz, Core cross-linked polymeric micelles for specific Iron delivery: inducing sterile inflammation in macrophages, Adv. Healthc. Mater. 10 (19) (2021) 2100385.
[28] G. Wang, N.J. Serkova, E.V. Groman, R.I. Scheinman, D. Simberg, Feraheme (Ferumoxytol) is recognized by Proinflammatory and anti-inflammatory macrophages via scavenger receptor type AI/II, Mol. Pharm. 16 (10) (2019) 4274–4281.
[29] M. Aghighi, A.J. Theruvath, A. Pareek, L.L. Pisani, R. Alford, A.M. Muehe, T. K. Sethi, S.J. Holdsworth, F.K. Hazard, D. Gratzinger, S. Luna-Fineman, R. Advani, S.L. Spunt, H.E. Daldrup-Link, Magnetic resonance imaging of tumor-associated macrophages: clinical translation, Clin. Cancer Res. 24 (17) (2018) 4110–4118.
[30] R.M. Pallares, F. Kiessling, T. Lammers, Bridging the gap between lab and clinic for nanodiagnostics, Nanomedicine (Lond.) 18 (5) (2023) 413–416.
[31] J.M. Metselaar, T. Lammers, Challenges in nanomedicine clinical translation, Drug Deliv. Transl. Res. 10 (3) (2020) 721–725.
[32] J.-N. May, S.K. Golombek, M. Baues, A. Dasgupta, N. Drude, A. Rix, D. Rommel, S. von Stillfried, L. Appold, R. Pola, M. Pechar, L. van Bloois, G. Storm, A.J. C. Kuehne, F. Gremse, B. Theek, F. Kiessling, T. Lammers, Multimodal and multiscale optical imaging of nanomedicine delivery across the blood-brain barrier upon sonopermeation, Theranostics 10 (4) (2020) 1948–1959.
[33] B. Theek, M. Baues, F. Gremse, R. Pola, M. Pechar, I. Negwer, K. Koynov, B. Weber, M. Barz, W. Jahnen-Dechent, G. Storm, F. Kiessling, T. Lammers, Histidine-rich glycoprotein-induced vascular normalization improves EPR-mediated drug targeting to and into tumors, J. Control. Release 282 (2018) 25–34.
[34] B.T.T. Pham, E.K. Colvin, N.T.H. Pham, B.J. Kim, E.S. Fuller, E.A. Moon, R. Barbey, S. Yuen, B.H. Rickman, N.S. Bryce, S. Bickley, M. Tanudji, S.K. Jones, V.M. Howell, B.S. Hawkett, Biodistribution and clearance of stable superparamagnetic maghemite iron oxide nanoparticles in mice following intraperitoneal administration, Int. J. Mol. Sci. 19 (1) (2018).
[35] D. Liu, W. Wu, J. Ling, S. Wen, N. Gu, X. Zhang, Effective PEGylation of Iron oxide nanoparticles for high performance in vivo Cancer imaging, Adv. Funct. Mater. 21 (8) (2011) 1498–1504.
[36] A. Antonelli, P. Szwargulski, E.-S. Scarpa, F. Thieben, G. Cordula, G. Ambrosi, L. Guidi, P. Ludewig, T. Knopp, M. Magnani, Development of long circulating magnetic particle imaging tracers: use of novel magnetic nanoparticles and entrapment into human erythrocytes, Nanomedicine 15 (8) (2020) 739–753.
[37] P.P.P. Kumar, M. Nafiujjaman, A.V. Makela, K. Hadrick, M.L. Hill, M. Lee, T. Kim, Development of Iron oxide Nanochains as a sensitive magnetic particle imaging tracer for Cancer detection, ACS Appl. Mater. Interfaces 17 (14) (2025) 20859–20871.
[38] S. Fütterer, I. Andrusenko, U. Kolb, W. Hofmeister, P. Langguth, Structural characterization of iron oxide/hydroxide nanoparticles in nine different parenteral drugs for the treatment of iron deficiency anaemia by electron diffraction (ED) and X-ray powder diffraction (XRPD), J. Pharm. Biomed. Anal. 86 (2013) 151–160.
[39] A. Remmo, D. Eberbeck, O. Kosch, L. Kampen, A. Ludwig, A.-N. Egler-Kemmerer, F. Wiekhorst, N. Loewa, Immobilization-induced anomalous dynamic magnetization effect in Synomag nanoparticles as tracers for magnetic particle imaging, ACS Appl. Nano Mater. 7 (21) (2024) 24315–24324.
[40] P. Zou, K. Tyner, A. Raw, S. Lee, Physicochemical characterization of Iron carbohydrate colloid drug products, AAPS J. 19 (5) (2017) 1359–1376.
[41] Y. Li, R.A. Barmin, R. Zhang, F. Kiessling, T. Lammers, R.M. Pallares, Clinical translation and landscape of superparamagnetic iron oxide nanoparticles, Adv. Drug Deliv. Rev. 229 (2026) 115756.
[42] J. Matuszak, P. Dörfler, J. Zaloga, H. Unterweger, S. Lyer, B. Dietel, C. Alexiou, I. Cicha, Shell matters: magnetic targeting of SPIONs and in vitro effects on endothelial and monocytic cell function, Clin. Hemorheol. Microcirc. 61 (2) (2015) 259–277.
[43] A. Janikowska, J. Matuszak, S. Lyer, E. Schreiber, H. Unterweger, J. Zaloga, J. Groll, C. Alexiou, I. Cicha, A novel human artery model to assess the magnetic accumulation of SPIONs under flow conditions, Sci. Rep. 7 (1) (2017) 42314.
[44] J.M. Rojas, L. Sanz-Ortega, V. Mulens-Arias, L. Gutiérrez, S. Pérez-Yagüe, D. F. Barber, Superparamagnetic iron oxide nanoparticle uptake alters M2 macrophage phenotype, iron metabolism, migration and invasion, Nanomedicine 12 (4) (2016) 1127–1138.
[45] J. Gu, H. Xu, Y. Han, W. Dai, W. Hao, C. Wang, N. Gu, H. Xu, J. Cao, The internalization pathway, metabolic fate and biological effect of superparamagnetic iron oxide nanoparticles in the macrophage-like RAW264.7 cell, Sci. China Life Sci. 54 (9) (2011) 793–805.
[46] H. Kang, S. Kim, D.S.H. Wong, H.J. Jung, S. Lin, K. Zou, R. Li, G. Li, V.P. Dravid, L. Bian, Remote manipulation of ligand Nano-oscillations regulates adhesion and polarization of macrophages in vivo, Nano Lett. 17 (10) (2017) 6415–6427.
[47] Y. Xu, X. Liu, Y. Li, H. Dou, H. Liang, Y. Hou, SPION-MSCs enhance therapeutic efficacy in sepsis by regulating MSC-expressed TRAF1-dependent macrophage polarization, Stem Cell Res. Ther. 12 (1) (2021) 531.
[48] N.K. Horvat, S. Chocarro, O. Marques, T.A. Bauer, R. Qiu, A. Díaz-Jimenez, B. Helm, Y. Chen, S. Sawall, R. Sparla, L. Su, U. Klingmuller, M. Barz, M. W. Hentze, R. Sotillo, M.U. Muckenthaler, Superparamagnetic Iron oxide nanoparticles reprogram the tumor microenvironment and reduce lung Cancer regrowth after Crizotinib treatment, ACS Nano 18 (17) (2024) 11025–11041.
[49] Q. Wu, R. Jin, T. Feng, L. Liu, L. Yang, Y. Tao, J.M. Anderson, H. Ai, H. Li, Iron oxide nanoparticles and induced autophagy in human monocytes, Int. J. Nanomedicine 12 (null) (2017) 3993–4005.
[50] M.R. Mohammadi, A.V. Malkovskiy, P. Jothimuthu, K.-M. Kim, M. Parekh, M. Inayathullah, Y. Zhuge, J. Rajadas, PEG/dextran double layer influences Fe ion release and colloidal stability of Iron oxide nanoparticles, Sci. Rep. 8 (1) (2018) 4286.
[51] M. Srinivas, P. Sharma, S. Jhunjhunwala, Phagocytic uptake of polymeric particles by immune cells under flow conditions, Mol. Pharm. 18 (12) (2021) 4501–4510.
[52] P. Sharma, A. Alakesh, S. Jhunjhunwala, The consequences of particle uptake on immune cells, Trends Pharmacol. Sci. 43 (4) (2022) 305–320.
[53] S. Hatamie, P.-J. Shih, B.-W. Chen, N. Hatami, Carbohydrate polymers, polymeric Nano drugs, and nanoparticles are used for advanced drug delivery and therapeutics in ocular diseases, Polym. Adv. Technol. 36 (2) (2025) e70094.
[54] H. Unterweger, L. Dézsi, J. Matuszak, C. Janko, M. Poettler, J. Jordan, T. Bäuerle, J. Szebeni, T. Fey, A.R. Boccaccini, C. Alexiou, I. Cicha, Dextran-coated superparamagnetic iron oxide nanoparticles for magnetic resonance imaging: evaluation of size-dependent imaging properties, storage stability and safety, Int. J. Nanomed. 13 (null) (2018) 1899–1915.
[55] A. Dubey, L. Izakelian, E.A. Ayaub, L. Ho, K. Stephenson, S. Wong, K. Kwofie, R. C. Austin, F. Botelho, K. Ask, C.D. Richards, Separate roles of IL-6 and oncostatin M in mouse macrophage polarization in vitro and in vivo, Immunol. Cell Biol. 96 (3) (2018) 257–272.
[56] L.-X. Tian, X. Tang, J.-Y. Zhu, W. Zhang, W.-Q. Tang, J. Yan, X. Xu, H.-P. Liang, Cytochrome P450 1A1 enhances Arginase-1 expression, which reduces LPS-induced mouse peritonitis by targeting JAK1/STAT6, Cell. Immunol. 349 (2020) 104047.
[57] G.P. Fadini, B.M. Bonora, R. Cappellari, L. Menegazzo, M. Vedovato, E. Iori, M. C. Marescotti, M. Albiero, A. Avogaro, Acute effects of Linagliptin on progenitor cells, monocyte phenotypes, and soluble mediators in type 2 diabetes, J. Clin. Endocrinol. Metabol. 101 (2) (2016) 748–756.

[58] S.N. Sunil Gowda, R. Raviraj, D. Nagarajan, W. Zhao, Radiation-induced lung injury: impact on macrophage dysregulation and lipid alteration – a review, Immunopharmacol. Immunotoxicol. 41 (3) (2019) 370–379.

[59] C. Laplagne, M. Domagala, A. Le Naour, C. Quemerais, D. Hamel, J.-J. Fournié, B. Couderc, C. Bousquet, A. Ferrand, M. Poupot, Latest advances in targeting the tumor microenvironment for tumor suppression, Int. J. Mol. Sci. 20 (19) (2019) 4719.

[60] R. Rydbirk, J. Folke, K. Winge, S. Aznar, B. Pakkenberg, T. Brudek, Assessment of brain reference genes for RT-qPCR studies in neurodegenerative diseases, Sci. Rep. 6 (1) (2016) 37116.

[61] L. Han, G. Lin, X. Lv, S. Li, Z. Huang, Y. Li, D. Chen, X. Chen, J. Lin, L. Chen, X. Lv, Exploring the potential value of Lactylation and macrophage polarization-related genes as biomarkers for TNF-α inhibitor response in inflammatory bowel disease, J. Inflamm. Res. 18 (2025) 18205–18228.

[62] M. Garelnabi, L.M. Taylor-Smith, E. Bielska, R.A. Hall, D. Stones, R.C. May, Quantifying donor-to-donor variation in macrophage responses to the human fungal pathogen Cryptococcus neoformans, PloS One 13 (3) (2018) e0194615.

[63] B. Taciak, A. Grochowska, M. Górczak, E. Górka, M. Skorzynski, M. Białasek, T. P. Rygiel, M. Król, Unveiling the phenotypic variability of macrophages: insights from donor diversity and pooling strategies, Int. J. Mol. Sci. 26 (3) (2025).

[64] C.G. Stirrat, S.R. Alam, T.J. MacGillivray, C.D. Gray, M.R. Dweck, J. Raftis, W. S. Jenkins, W.A. Wallace, R. Pessotto, K.H. Lim, S. Mirsadraee, P.A. Henriksen, S. I. Semple, D.E. Newby, Ferumoxytol-enhanced magnetic resonance imaging assessing inflammation after myocardial infarction, Heart 103 (19) (2017) 1528–1535.

[65] S.S. Hedgire, M. Shaunagh, W.G. R., A.S. Mahdi, H. Mukesh, J.L. Gaglia, Evaluation of renal quantitative T2* changes on MRI following administration of ferumoxytol as a T2* contrast agent, Int. J. Nanomed. 9 (2014) 2101–2107.

[66] M. Aghighi, L. Pisani, A.J. Theruvath, A.M. Muehe, J. Donig, R. Khan, S. J. Holdsworth, N. Kambham, W. Concepcion, P.C. Grimm, H.E. Daldrup-Link, Ferumoxytol is not retained in kidney allografts in patients undergoing acute rejection, Mol. Imaging Biol. 20 (1) (2018) 139–149.

[67] A. Sacco, A.M. Battaglia, C. Botta, I. Aversa, S. Mancuso, F. Costanzo, F. Biamonte, Iron metabolism in the tumor microenvironment—implications for anti-Cancer immune response, Cells 10 (2) (2021) 303.

[68] M.G. Ledesma-Colunga, U. Baschant, H. Weidner, T.C. Alves, P. Mirtschink, L. C. Hofbauer, M. Rauner, Transferrin receptor 2 deficiency promotes macrophage polarization and inflammatory arthritis, Redox Biol. 60 (2023) 102616.

[69] A.A. Kapralov, Q. Yang, H.H. Dar, Y.Y. Tyurina, T.S. Anthonymuthu, R. Kim, C. M. St. Croix, K. Mikulska-Ruminska, B. Liu, I.H. Shrivastava, V.A. Tyurin, H.-C. Ting, Y.L. Wu, Y. Gao, G.V. Shurin, M.A. Artyukhova, L.A. Ponomareva, P. S. Timashev, R.M. Domingues, D.A. Stoyanovsky, J.S. Greenberger, R. K. Mallampalli, I. Bahar, D.I. Gabrilovich, H. Bayır, V.E. Kagan, Redox lipid reprogramming commands susceptibility of macrophages and microglia to ferroptotic death, Nat. Chem. Biol. 16 (3) (2020) 278–290.

[70] L. Ma, F. Fang, H. Wang, P. Zhao, H. Yu, X. Liu, Macrophage co-culture promotes cell reprogramming and prevents ferroptosis in aging fibroblasts for neurodegeneration therapy, J. Mol. Med. 103 (3) (2025) 301–310.

[71] C. Yang, S. Li, L. Wang, Engineered iron oxide nanoplatforms: reprogramming immunosuppressive niches for precision cancer theranostics, Mol. Cancer 24 (1) (2025) 225.

[72] M. De Palma, C. Murdoch, M.A. Venneri, L. Naldini, C.E. Lewis, Tie2-expressing monocytes: regulation of tumor angiogenesis and therapeutic implications, Trends Immunol. 28 (12) (2007) 519–524.

[73] K.-X. Yu, W.-J. Yuan, H.-Z. Wang, Y.-X. Li, Extracellular matrix stiffness and tumor-associated macrophage polarization: new fields affecting immune exclusion, Cancer Immunol. Immunother. 73 (6) (2024) 115.

[74] K. Binnemars-Postma, G. Storm, J. Prakash, Nanomedicine strategies to target tumor-associated macrophages, Int. J. Mol. Sci. 18 (5) (2017) 979.

[75] E.A. Vermeij, M.I. Koenders, M.B. Bennink, L.A. Crowe, L. Maurizi, J.-P. Vallée, H. Hofmann, W.B. van den Berg, P.L.E.M. van Lent, F.A.J. van de Loo, The in-vivo use of superparamagnetic Iron oxide nanoparticles to detect inflammation elicits a cytokine response but does not aggravate experimental arthritis, PloS One 10 (5) (2015) e0126687.

[76] H. Vu-Quang, M.-K. Yoo, H.-J. Jeong, H.-J. Lee, M. Muthiah, J.H. Rhee, J.-H. Lee, C.-S. Cho, Y.Y. Jeong, I.-K. Park, Targeted delivery of mannan-coated superparamagnetic iron oxide nanoparticles to antigen-presenting cells for magnetic resonance-based diagnosis of metastatic lymph nodes in vivo, Acta Biomater. 7 (11) (2011) 3935–3945.

[77] A.P. Klapproth, M. Shevtsov, S. Stangl, W.B. Li, G. Multhoff, A new pharmacokinetic model describing the biodistribution of intravenously and intratumorally administered superparamagnetic iron oxide nanoparticles (SPIONs) in a GL261 xenograft glioblastoma model, Int. J. Nanomed. 15 (2020) 4677–4689.

[78] L. Wise-Faberowski, N. Velasquez, F. Chan, S. Vasanawala, D.B. McElhinney, C. Ramamoorthy, Safety of ferumoxytol in children undergoing cardiac MRI under general anaesthesia, Cardiol. Young 28 (7) (2018) 916–921.

[79] A.M. Muehe, D. Feng, R. von Eyben, S. Luna-Fineman, M.P. Link, T. Muthig, A. E. Huddleston, E.A. Neuwelt, H.E. Daldrup-Link, Safety report of Ferumoxytol for magnetic resonance imaging in children and young adults, Invest. Radiol. 51 (4) (2016) 221–227.

[80] M. Gkagkanasiou, A. Ploussi, M. Gazouli, E.P. Efstathopoulos, USPIO-enhanced MRI neuroimaging: a review, J. Neuroimaging 26 (2) (2016) 161–168.

[81] J. Blöck, L. Imschweiler, R. Mihyar, J. Chen, R. Barmin, S. Koletnik, R.M. Pallares, T. Lammers, A. Rix, F. Kiessling, Ultrasound-activated poly(butyl cyanoacrylate) microbubbles enhance the therapeutic effect of Doxil, Pharmacol. Res. 219 (2025) 107916.

[82] A. Banerjee, R. Bandopadhyay, Use of dextran nanoparticle: a paradigm shift in bacterial exopolysaccharide based biomedical applications, Int. J. Biol. Macromol. 87 (2016) 295–301.

[83] H. Kuroda, T. Jamiyan, R. Yamaguchi, A. Kakumoto, A. Abe, O. Harada, A. Masunaga, Tumor microenvironment in triple-negative breast cancer: the correlation of tumor-associated macrophages and tumor-infiltrating lymphocytes, Clin. Transl. Oncol. 23 (12) (2021) 2513–2525.

[84] M. Panagi, C. Voutouri, F. Mpekris, P. Papageorgis, M.R. Martin, J.D. Martin, P. Demetriou, C. Pierides, C. Polydorou, A. Stylianou, M. Louca, L. Koumas, P. Costeas, K. Kataoka, H. Cabral, T. Stylianopoulos, TGF-β inhibition combined with cytotoxic nanomedicine normalizes triple negative breast cancer microenvironment towards anti-tumor immunity, Theranostics 10 (4) (2020) 1910–1922.

[85] B. Theek, F. Gremse, S. Kunjachan, S. Fokong, R. Pola, M. Pechar, R. Deckers, G. Storm, J. Ehling, F. Kiessling, T. Lammers, Characterizing EPR-mediated passive drug targeting using contrast-enhanced functional ultrasound imaging, J. Control. Release 182 (2014) 83–89.

[86] S. Kunjachan, F. Gremse, B. Theek, P. Koczera, R. Pola, M. Pechar, T. Etrych, K. Ulbrich, G. Storm, F. Kiessling, T. Lammers, Noninvasive optical imaging of nanomedicine biodistribution, ACS Nano 7 (1) (2013) 252–262.

[87] T. Lammers, P. Peschke, R. Kühnlein, V. Subr, K. Ulbrich, J. Debus, P. Huber, W. Hennink, G. Storm, Effect of radiotherapy and hyperthermia on the tumor accumulation of HPMA copolymer-based drug delivery systems, J. Control. Release 117 (3) (2007) 333–341.

[88] N. Yang, Z. Ye, F. Li, R.I. Mahato, HPMA polymer-based site-specific delivery of oligonucleotides to hepatic stellate cells, Bioconjug. Chem. 20 (2) (2009) 213–221.

[89] L. Harkins, S. Vilarinho, W.M. Saltzman, Targeting polymeric nanoparticles to specific cell populations in the liver, Biochemistry 64 (8) (2025) 1685–1697.

[90] S. Sadekar, A. Ray, M. Janàt-Amsbury, C.M. Peterson, H. Ghandehari, Comparative biodistribution of PAMAM dendrimers and HPMA copolymers in ovarian-tumor-bearing mice, Biomacromolecules 12 (1) (2011) 88–96.

[91] D.-Y. Chang, J.P. Speth, M.L. Scarpelli, Evaluating the theranostic potential of ferumoxytol when combined with radiotherapy in a mammary dual tumor mouse model, Med. Phys. 52 (7) (2025) e17888.

[92] L.O. Sillerud, A.J. Neuwelt, F.I. Staquicini, W. Arap, R. Pasqualini, Repurposing Ferumoxytol as a breast Cancer-associated macrophage tracer with five-dimensional quantitative [Fe]MRI of SPION dynamics, Cancers 13 (15) (2021) 3802.

[93] H. Specht, E. Emmott, A.A. Petelski, R.G. Huffman, D.H. Perlman, M. Serra, P. Kharchenko, A. Koller, N. Slavov, Single-cell proteomic and transcriptomic analysis of macrophage heterogeneity using SCoPE2, Genome Biol. 22 (1) (2021) 50.

[94] J. Yu, C. Shang, X. Deng, J. Jia, X. Shang, Z. Wang, Y. Zheng, R. Zhang, Y. Wang, H. Zhang, H. Liu, W.J. Liu, H. Li, B. Cao, Time-resolved scRNA-seq reveals transcription dynamics of polarized macrophages with influenza a virus infection and antigen presentation to T cells, Emerg. Microbes Infections 13 (1) (2024) 2387450.

[95] Y. Saimoto, D. Kusakabe, K. Morimoto, Y. Matsuoka, E. Kozakura, N. Kato, K. Tsunematsu, T. Umeno, T. Kiyotani, S. Matsumoto, M. Tsuji, T. Hirayama, H. Nagasawa, K. Uchida, S. Karasawa, M. Jutanom, K.-I. Yamada, Lysosomal lipid peroxidation contributes to ferroptosis induction via lysosomal membrane permeabilization, Nat. Commun. 16 (1) (2025) 3554.

[96] R. Namgung, K. Singha, M.K. Yu, S. Jon, Y.S. Kim, Y. Ahn, I.-K. Park, W.J. Kim, Hybrid superparamagnetic iron oxide nanoparticle-branched polyethylenimine magnetoplexes for gene transfection of vascular endothelial cells, Biomaterials 31 (14) (2010) 4204–4213.

[97] J. Choi, D.-I. Kim, J.-Y. Kim, S. Pané, B.J. Nelson, Y.-T. Chang, H. Choi, Magnetically enhanced intracellular uptake of superparamagnetic Iron oxide nanoparticles for antitumor therapy, ACS Nano 17 (16) (2023) 15857–15870.

[98] S.H. Lee, D.J. Park, W.S. Yun, J.-E. Park, J.S. Choi, J. Key, Y.J. Seo, Endocytic trafficking of polymeric clustered superparamagnetic iron oxide nanoparticles in mesenchymal stem cells, J. Control. Release 326 (2020) 408–418.

[99] L. Zhu, J. Hu, X. Wu, J. Zhang, X. Xu, X. Huang, B. Tian, C.-X. Zhao, Y. Du, L. Wu, Programmed enhancement of endogenous iron-mediated lysosomal membrane permeabilization for tumor ferroptosis/pyroptosis dual-induction, Nat. Commun. 16 (1) (2025) 3017.

[100] T. Yamashima, Lysosomal membrane-permeabilization (LMP) and -rupture (LMR) are distinct for cell death, Front. Cell Death 4 (2025).

[101] K.-S. Kim, B. Choi, H. Choi, M.J. Ko, D.-H. Kim, D.-H. Kim, Enhanced natural killer cell anti-tumor activity with nanoparticles mediated ferroptosis and potential therapeutic application in prostate cancer, J. Nanobiotechnol. 20 (1) (2022) 428.

[102] S. Wang, M. Cheng, P. Peng, Y. Lou, A. Zhang, P. Liu, Iron released after Cryo-thermal therapy induced M1 macrophage polarization, promoting the differentiation of CD4+ T cells into CTLs, Int. J. Mol. Sci. 22 (13) (2021) 7010.

[103] S. Baroni, M.R. Ruggiero, V. Bitonto, L.M. Broche, D.J. Lurie, S. Aime, S. Geninatti Crich, In vivo assessment of tumour associated macrophages in murine melanoma obtained by low-field relaxometry in the presence of iron oxide particles, Biomaterials 236 (2020) 119805.

[104] S. Sun, J. Shen, J. Jiang, F. Wang, J. Min, Targeting ferroptosis opens new avenues for the development of novel therapeutics, Signal Transduct. Target. Ther. 8 (1) (2023) 372.

[105] Y. Pan, J. Li, X. Xia, J. Wang, Q. Jiang, J. Yang, H. Dou, H. Liang, K. Li, Y. Hou, β-Glucan-coupled superparamagnetic iron oxide nanoparticles induce trained immunity to protect mice against sepsis, Theranostics 12 (2) (2022) 675–688.
[106] R. Jin, L. Liu, W. Zhu, D. Li, L. Yang, J. Duan, Z. Cai, Y. Nie, Y. Zhang, Q. Gong, B. Song, L. Wen, J.M. Anderson, H. Ai, Iron oxide nanoparticles promote macrophage autophagy and inflammatory response through activation of toll-like Receptor-4 signaling, Biomaterials 203 (2019) 23–30.
[107] Y. Sato, Y. Fu, H. Liu, M.Y. Lee, M.H. Shaw, Tumor-immune profiling of CT-26 and Colon 26 syngeneic mouse models reveals mechanism of anti-PD-1 response, BMC Cancer 21 (1) (2021) 1222.
[108] B.L. Daugherty, Abstract 704: MDSC-targeted TFF2-MSA suppresses tumor growth and increases survival in anti-PD-1 treated MC38 and CT26.Wt murine colorectal cancer models, Cancer Res. 83 (7_Supplement) (2023) 704.
[109] K.P. Fabian, M.R. Padget, R. Fujii, J. Schlom, J.W. Hodge, Differential combination immunotherapy requirements for inflamed (warm) tumors versus T cell excluded (cool) tumors: engage, expand, enable, and evolve, J. Immunother. Cancer 9 (2) (2021).
[110] C. Kim, J.-Y. Suh, C. Heo, C.K. Lee, W.H. Shim, B.W. Park, G. Cho, D.-W. Lee, D.-C. Woo, S.-Y. Kim, Y.J. Kim, D.-J. Bae, J.K. Kim, Spatiotemporal heterogeneity of tumor vasculature during tumor growth and antiangiogenic treatment: MRI assessment using permeability and blood volume parameters, Cancer Med. 7 (8) (2018) 3921–3934.
[111] V. Trujillo-Alonso, E.C. Pratt, H. Zong, A. Lara-Martinez, C. Kaittanis, M.O. Rabie, V. Longo, M.W. Becker, G.J. Roboz, J. Grimm, M.L. Guzman, FDA-approved ferumoxytol displays anti-leukaemia efficacy against cells with low ferroportin levels, Nat. Nanotechnol. 14 (6) (2019) 616–622.
[112] T.J. Carter, G. Agliardi, F.-Y. Lin, M. Ellis, C. Jones, M. Robson, A. Richard-Londt, P. Southern, M. Lythgoe, M. Zaw Thin, V. Ryzhov, R.T.M. de Rosales, C. Gruettner, M.R.A. Abdollah, R.B. Pedley, Q.A. Pankhurst, T.L. Kalber, S. Brandner, S. Quezada, P. Mulholland, M. Shevtsov, K. Chester, Potential of magnetic hyperthermia to stimulate localized immune activation, Small 17 (14) (2021) 2005241.
[113] C. Pucci, A. Degl'Innocenti, M. Belenli Gümüş, G. Ciofani, Superparamagnetic iron oxide nanoparticles for magnetic hyperthermia: recent advancements, molecular effects, and future directions in the omics era, Biomater. Sci. 10 (9) (2022) 2103–2121.
[114] L. Zhou, C. Dong, L. Ding, W. Feng, L. Yu, X. Cui, Y. Chen, Targeting ferroptosis synergistically sensitizes apoptotic sonodynamic anti-tumor nanotherapy, Nano Today 39 (2021) 101212.
[115] J. Sharkey, P.J. Starkey Lewis, M. Barrow, S.M. Alwahsh, J. Noble, E. Livingstone, R.J. Lennen, M.A. Jansen, J.G. Carrion, N. Liptrott, S. Forbes, D.J. Adams, A. E. Chadwick, S.J. Forbes, P. Murray, M.J. Rosseinsky, C.E. Goldring, B.K. Park, Functionalized superparamagnetic iron oxide nanoparticles provide highly efficient iron-labeling in macrophages for magnetic resonance–based detection in vivo, Cytotherapy 19 (4) (2017) 555–569.
[116] A.B. Mathiasen, L. Hansen, T. Friis, C. Thomsen, K. Bhakoo, J. Kastrup, Optimal labeling dose, labeling time, and magnetic resonance imaging detection limits of Ultrasmall superparamagnetic Iron-oxide nanoparticle labeled mesenchymal stromal cells, Stem Cells Int. 2013 (1) (2013) 353105.
[117] S. Stoumpos, M. Hennessy, A.T. Vesey, A. Radjenovic, R. Kasthuri, D. B. Kingsmore, P.B. Mark, G. Roditi, Ferumoxytol magnetic resonance angiography: a dose-finding study in patients with chronic kidney disease, Eur. Radiol. 29 (7) (2019) 3543–3552.
[118] M.R. Bashir, L. Bhatti, D. Marin, R.C. Nelson, Emerging applications for ferumoxytol as a contrast agent in MRI, J. Magn. Reson. Imaging 41 (4) (2015) 884–898.
[119] R. van der Meel, E. Sulheim, Y. Shi, F. Kiessling, W.J.M. Mulder, T. Lammers, Smart cancer nanomedicine, Nat. Nanotechnol. 14 (11) (2019) 1007–1017.
[120] R.M. Pallares, L. Consolino, A. Wang, F. De Lorenzi, F. Kiessling, A. Schroeder, T. Lammers, Targeting metastasis with nanomedicine, Nat. Rev. Bioeng. 4 (2026) 47–66.
[121] J.C. Sachdev, P. Munster, D.W. Northfelt, H.S. Han, C. Ma, F. Maxwell, T. Wang, B. Belanger, B. Zhang, Y. Moore, A. Thiagalingam, C. Anders, Phase I study of liposomal irinotecan in patients with metastatic breast cancer: findings from the expansion phase, Breast Cancer Res. Treat. 185 (3) (2021) 759–771.